DTU Library

Unmanned Aerial System (UAS) observations of water surface elevation in a small stream

Comparison of radar altimetry, LIDAR and photogrammetry techniques

Bandini, Filippo; Sunding, Tanya Pheiffer; Linde, Johannes; Smith, Ole; Jensen, Inger Klint; Köppl, Christian Josef; Butts, Michael; Bauer-Gottwein, Peter

Published in:
Remote Sensing of Environment

Link to article, DOI:
10.1016/j.rse.2019.111487

Publication date:
2020

Document Version
Peer reviewed version

Citation (APA):
Bandini, F., Sunding, T. P., Linde, J., Smith, O., Jensen, I. K., Köppl, C. J., Butts, M., & Bauer-Gottwein, P. (2020). Unmanned Aerial System (UAS) observations of water surface elevation in a small stream: Comparison of radar altimetry, LIDAR and photogrammetry techniques. *Remote Sensing of Environment*, *237*, Article 111487. https://doi.org/10.1016/j.rse.2019.111487

Unmanned Aerial System (UAS) observations of water surface elevation in a small stream: comparison of radar altimetry, LIDAR and photogrammetry techniques.

Filippo Bandini[1*], Tanya Pheiffer Sunding[1], Johannes Linde[2], Ole Smith[3], Inger Klint Jensen[3], Christian Josef Köppl[1], Michael Butts[4], Peter Bauer-Gottwein[1].

*Corresponding author at: Department of Environmental Engineering, Technical University of Denmark, Bygning 115, 2800 Kgs. Lyngby, Denmark. E-mail address: fban@env.dtu.dk

[1]Department of Environmental Engineering, Technical University of Denmark, Bygning 115, 2800 Kgs. Lyngby, Denmark.

[2]DTU Space, National Space Institute, Elektrovej, building 328, 2800 Kgs. Lyngby, Denmark.

[3]Orbicon, A/S, Høje-Taastrup, Linnés Allé 2, 2630 Taastrup, Denmark.

[4]Water Resources Department, DHI, 2970 Hoersholm, Denmark

Keywords: UAS, LIDAR, radar, photogrammetry, water level, water surface elevation

Abstract

Water Surface Elevation (WSE) is an important hydrometric observation, useful to calibrate hydrological models, predict floods, and assess climate change. However, the number of in-situ gauging stations is in decline worldwide. Satellite altimetry, including the recently launched satellite missions (e.g. the radar altimetry missions Cryosat 2, Jason 3, Sentinel 3A/B and the LIDAR mission ICESat-2), can determine WSE only in rivers which are more than ca. 100 m wide. WSE measurements in small streams currently remain limited to the few existing in-situ stations or to time-consuming in-situ surveys. Unmanned Aerial Systems (UAS) can acquire real-time WSE observations during periods of hydrological interest (but with flight limitations in extreme weather conditions), within short survey times and with automatic or semi-automatic flight operations. UAS-borne photogrammetry is a well-known technique that can estimate land elevation with an accuracy as high as a few cm, similarly UAS-borne LIDAR can estimate land elevation but without requiring Ground Control Points (GCPs). However, both techniques face limitations in estimating WSE: water transparency and lack of stable visual key points on the Water Surface (WS) complicate the UAS-borne photogrammetric estimates of WSE, while the LIDAR reflection from the water surface is generally not strong enough to be captured by most of the UAS-borne LIDAR systems currently available on the market. Thus, LIDAR and photogrammetry generally require extraction of the elevation of the "water-edge" points, i.e. points at the interface between land and water, for identifying the WSE. We demonstrate highly accurate WSE observations with a new radar altimetry solution, which comprises a 77 GHz radar chip with full waveform analysis and an accurate dual frequency differential Global Navigation Satellite System (GNSS) system. The radar altimetry solution shows the lowest standard deviation (σ) and RMSE on WSE estimates, ca. 1.5 cm and ca. 3 cm respectively, whilst photogrammetry and LIDAR show a σ and an RMSE at decimetre level. Radar altimetry also requires a significantly shorter survey and processing time compared to LIDAR and especially to photogrammetry.

1. Introduction

According to Tauro et al. (2018) new measurement techniques, equipment and sensors are needed to characterize the hydrological cycle. The global decline of measuring stations and systems for hydrology continues (Lawford et al., 2013). However, in recent years, there has been a general trend towards data mining and hydrological modelling rather than experimental research (Blume et al., 2017; Sidle, 2006). Accurate and high spatial resolution observations of water surface elevation (WSE) are essential for validation and calibration of hydraulic models (Giustarini et al., 2011; Langhammer et al., 2017; Tarpanelli et al., 2013) and for flood forecasting (Asadzadeh Jarihani et al., 2013; Domeneghetti, 2016; Montesarchio et al., 2015). Hydrodynamic models would require spatially distributed calibration and validation of WSE (Alsdorf et al., 2007), however in-situ campaigns or gauge stations can retrieve only point-based measurements and do not ensure the adequate spatial coverage to characterize the river networks.

Conversely, spaceborne WSE measurements are currently constrained by the spatial and temporal resolutions of satellite altimeters, with a vertical accuracy of decimetres to meters (Asadzadeh Jarihani et al., 2013; Biancamaria et al., 2017; Calmant and Seyler, 2006). The upcoming SWOT mission (Durand et al., 2010; Neeck et al., 2012) is expected to provide 2D measurements of WSEs for many of the world's prominent rivers, lakes, and wetlands with decimetre-level accuracy over 1 km^2 areas (Biancamaria et al., 2016; Pavelsky et al., 2014). Altenau et al. (2017) demonstrated that AirSWOT, an airborne instrument that produces radar measurements analogous to SWOT, can obtain observations with an RMSE of 9.0 cm for WSEs averaged over 1 km^2 areas and 1.0 cm/km for slopes along 10 km reaches. However, the spaceborne SWOT is expected to be capable of monitoring only rivers whose width exceeds 100 m (https://earth.esa.int/web/eoportal/satellite-missions/s/swot), therefore is not expected to deliver WSE observations of small rivers (less than 100 m), which remain currently ungauged by satellite observations. However, small rivers are an essential part of the river network, because they govern connectivity at the watershed-scale (e.g.

Wohl, 2017), constitute the whole river network in some geographical regions or countries and can cause major floods in both rural and urban areas.

Manned aerial LIDAR instruments can measure WSE and slope also in small rivers. However, accurate determination of the water surface (WS) is not trivial for LIDAR instruments (Guenther, 1981). WSE can be extracted from the “water-edges” of the LIDAR point cloud with a vertical accuracy at the decimetre level (Legleiter, 2012), or in case LIDAR instruments have a suitable frequency, pulse energy and pulse width for directly detecting the WS, WSE can be directly measured with an accuracy from few cm to a few tens of cm (Hopkinson et al., 2011; Schumann et al., 2008). Generally, Near-Infrared (NIR) is reflected by the air-water interface and does not penetrate below the WS, while blue/green LIDAR pulses penetrate below the WS and travel through the water column (e.g. Andersen et al., 2017). Because the green water surface returns include returns from the air–water interface but also from the volume backscatter and the bed, Guenther et al. (2000) suggested to avoid the use of green LIDAR for measuring the WS. On the other hand, the use of NIR LIDAR data for WS detection is documented in several studies (e.g. Allouis et al., 2010; Brzank et al., 2008; Collin et al., 2008; Höfle et al., 2009).

Compared to manned aircrafts, Unmanned Aerial Systems (UAS) are low cost, portable flight platforms that can ensure inexpensive and versatile flight operations. UAS can fly at a lower altitude, i.e. closer to the stream, and can be deployed at short notice, for example during a period of hydrological interest. UAS are customizable with different payloads, but with limited size and weight available for the sensors, which significantly limits the availability of UAS-borne LIDAR systems. Mandlburger et al. (2016) tested the novel topo-bathymetric laser profiler system (RIEGLBDF-1) onboard RIEGL BathyCopter (RIEGL, Austria). This LIDAR system implements a green wavelength and is able to detect WS and also bathymetry (penetration up to 1.5 Secchi depth). The authors demonstrated that the system can measure WSE, with a median vertical error of ca. 4.5 cm, mainly due to penetration of green LIDAR below the WS. Furthermore, the authors report a standard deviation of 6 cm in measurements, which was assumed to be caused by the short-term variability of the WS (e.g. roughness). The authors specified that a combined NIR/green LIDAR solution would be optimal for WS detection.

Huang et al. (2018) tested a lightweight and relatively cheap scanning laser (UTM-30LX, Hokuyo Automatic Co., LTD., Japan) onboard a UAS to measure WSE of the sea, including wave heights. The NIR laser system could receive only 10%–35% of useful data returns from a height of 6 m over the sea, and for this reason, it was operated at altitudes of 6–10 m above sea level. The vertical RMSE in sea WSE observation was 5 cm for a flight height of 10 m in hover mode. The major factors affecting system accuracy were the accuracy of i) the Inertial Measurement Unit (IMU), ii) the Real Time Kinematic (RTK) Global Navigation Satellite System (GNSS) system, iii) the scanning laser and iv) the synchronization between the sensors.

Due to the weight and price of airborne LIDAR systems, in recent years researchers have experimented with UAS-photogrammetry to measure WSE. Photogrammetric Digital Elevation Models (DEMs) can generally estimate the elevation of solid surfaces with a vertical accuracy of few cm (Bühler et al., 2017; Carbonneau and Dietrich, 2017; Ouédraogo et al., 2014; Santise et al., 2014). However, WS is notoriously difficult to reproduce: shadows, aquatic vegetation, lack of stable visual key points on the WS, and through-water penetration of visible light complicate the reconstruction of the WS with Structure-from-Motion (SfM) algorithms. Westaway et al. (2001, 2000) suggested that WS maps could be produced by interpolating WS information from data points acquired from dry locations ("water-edge") adjacent to inundated areas. Using this "water-edge" technique, Woodget et al (2015) have demonstrated that WSE can be estimated by i) visually identifying the "water-edge" interface on the UAS-orthophoto and ii) extracting the elevation of the "water-edge" at small intervals from the digital surface map derived from UAS-imagery. The "water-edge" can be successfully identified along streambanks which exhibit clearly identifiable edges (e.g. vegetation does not protrude over the stream) and gentle bank slopes (Javernick et al., 2014; Pai et al., 2017). Different automatic algorithms have been developed to identify the "water-edge", particularly on images captured by in-situ static optical camera, e.g. supervised methods (Young et al., 2015) based on Canny's edge detection algorithm (Canny, 1986), or similarly methods based on analysis of grey-scale image profiles to detect the water-solid surface transition signal (Leduc et al., 2018). Pai et al. (2017) attempted to identify the "water-edge" on UAS-imagery via Normalized Water Difference Index (NDVI) or NIR thresholds estimated from multispectral images, but did not report a substantial improvement compared to visual identification. Ridolfi and Manciola (2018) proved that the "water-edge" between WS and the solid surface constituting a dam can be clearly identified on UAS-imagery via Canny algorithms.

The accuracy of WSE observations estimated via photogrammetric techniques depends on the accuracy of the photogrammetric DEM and on "water-edge" identification accuracy. In general, photogrammetry requires high computational power and time-consuming human-computer interaction to visually identify the ground control points (GCPs) and inspect the "water-edge" points.

Given the current limitations of LIDAR and photogrammetry systems, Bandini et al. (2017b) retrieved WSE observations of a lake with different UAS-sensors, i.e. sonar system, radar and camera-laser based prototype, in order to test precision, accuracy and beam divergence of each of the sensors. The radar system was demonstrated to provide a ranging accuracy of ca. 0.5% of range. With GNSS system delivering a vertical accuracy better than 3-5 cm, the radar-GNSS system was proven to measure WSE of the lake with an overall accuracy better than 5–7 cm.

In this paper, we describe a new UAS-based radar altimetry solution with full waveform analysis, together with LIDAR and photogrammetric methods. The performance of a LIDAR, photogrammetric and radar estimates of WSE are quantified and compared to an independent conventional manual gauging in a small stream reach. The advantages and limitations of the different sensor technologies are reviewed, and both the accuracy and operating costs compared. We find that the radar observations are approximately an order of magnitude better than either LIDAR or photogrammetry.

2. Materials and methods

Firstly, this study aims to show that UAS-borne WSE measurements retrieved with an innovative full waveform radar system are more reliable and accurate than photogrammetry or LIDAR WSE estimates. Secondly, the study aims to demonstrate the applicability of this UAS-borne radar technique with full waveform analysis also in a very small stream (1-2 m wide) that is fully covered by dense vegetation over most of its length.

To demonstrate this, UAS-borne WSE observations were retrieved in two case studies:

i) in a ca. 2.3 km stretch of the stream Åmose Å (Denmark) on November 21, 2018. This stretch had a WS width of ca. 3-4 m and was overhung by sparse deciduous trees. This campaign shows a comparison of UAS-borne estimates from the 3 different techniques, i.e. radar, LIDAR and photogrammetry, benchmarked with ground-truth observations.

ii) In a ca. 0.8 km stretch of the stream Nivå Å (Denmark) on June 25, 2019. This stretch had a WS maximum width of only 1.5-2 m. The stretch is almost fully covered by dense canopy: this survey shows that the radar altimetry solution with full waveform can identify the WS also in locations where the WS is not visible with optical imagery (e.g. photogrammetry) because the WS is fully covered by trees during their growth season.

This campaign shows the radar observations benchmarked with ground-truth observations.

Fig. 1 shows the location of the 2 streams, while Table 1 summarizes the morphological and hydraulic characteristics of the 2 river stretches.

Table 1, morphological and hydraulic characteristics of the 2 river stretches

Stream name	Coordinates Latitude/Longitude (WGS84) Total length:	Annual average WSE slope	Mean annual discharge	Maximum water depth	Water turbidity	Mean water surface width	Vegetation status
Åmose Å	From 55.566056/ 11.644617 To 55.567107/ 11.672163 Total length: 2.3 km	0.2-0.5 per mille	ca. 0.8 m^3/s, large annual variation	Ca. 1.5 m	High turbidity. Secchi depth: ca. 0.7 m	2-4 m	• Sparse riparian vegetation • Dense aquatic vegetation
Nivå Å	From 55.93008/ 12.48708 To	0.1-0.2 per mille	ca. 0.2 m^3/s, large	Ca. 0.6 m	Secchi depth: ca. 1-1.2 m	1-2 m	• Very dense riparian

	55.92900/ 12.49894 Total length: 0.8 km		annual variation				vegetation overhanging the stream • Dense aquatic vegetation

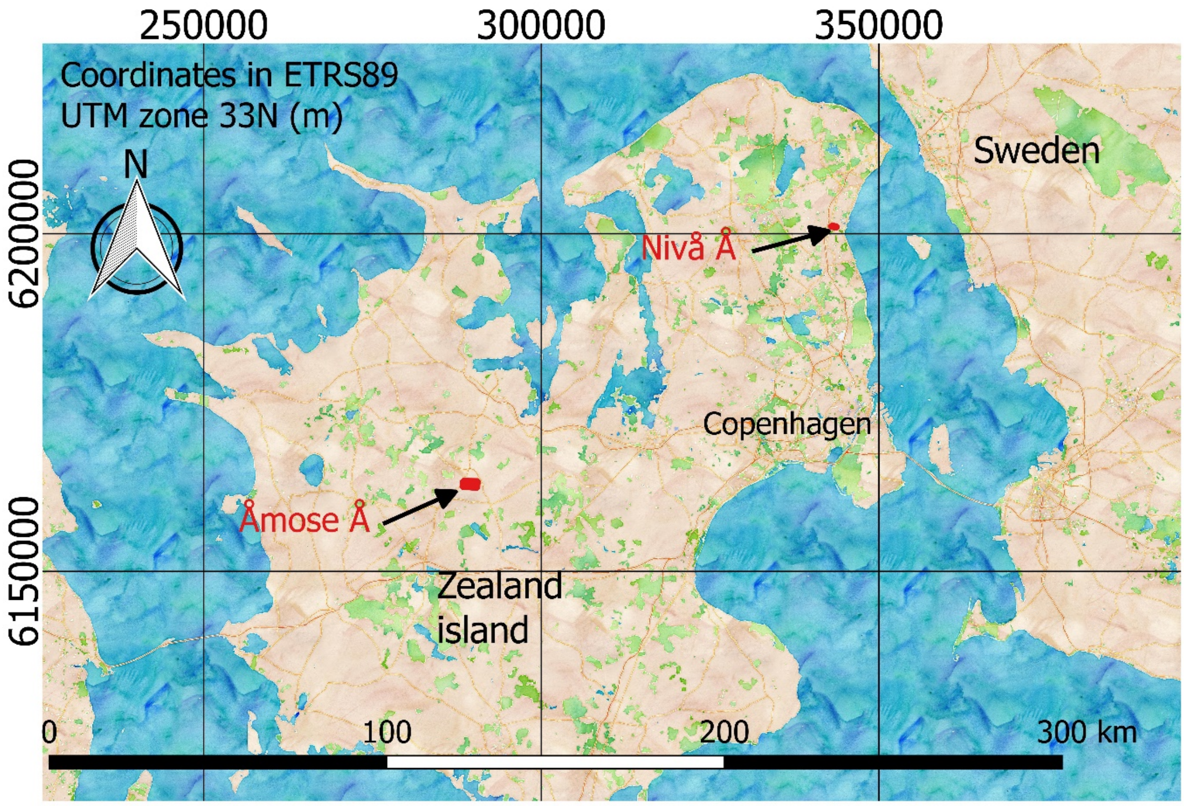

Fig. 1, General map of Zealand island (Denmark) with the location of the two stretches. Map tiles by Stamen Design, with Data by OpenStreetMap (Maps.stamen.com, 2019).

2.1. Åmose Å case study

Observations in Åmose Å were retrieved with our radar altimetry solution, a LIDAR system and UAS-borne photogrammetry. The flight paths for LIDAR and radar are shown in Fig. 2, while the flight path for photogrammetry is shown in Fig. 3.

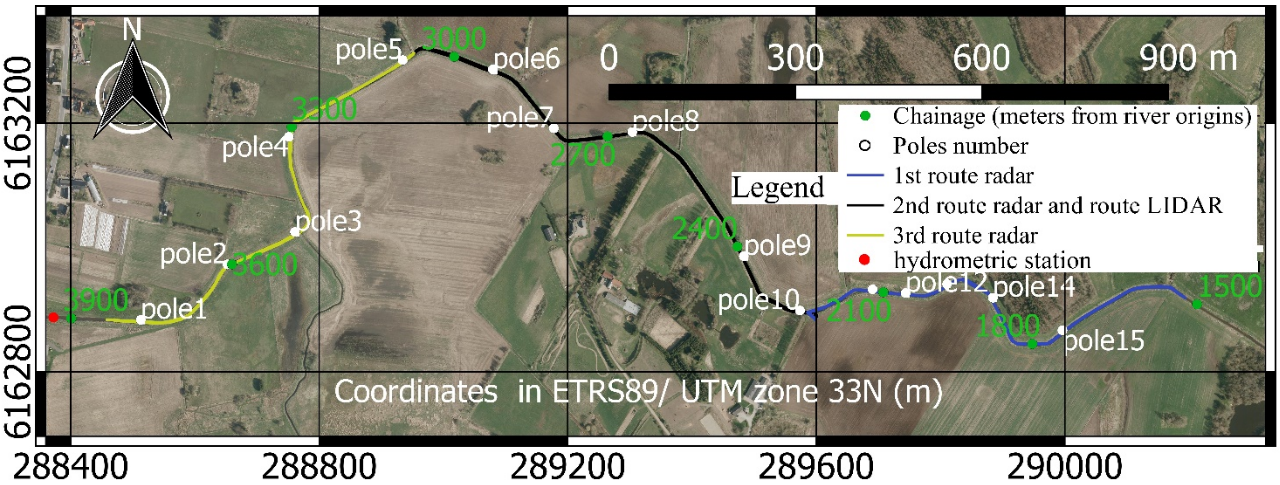

Fig. 2. Map showing the surveyed Åmose Å stretch and its corresponding chainage, which is the linear distance along watercourse from stream origin. The map includes the location of the poles used to retrieve in-situ measurements and the route flown by both the radar and the LIDAR. The red dot shows an in-situ gauging station to measure WSE. Map background is an orthophoto from the Danish Geodata Agency (Styrelsen for Dataforsyning og Effektivisering, 2018).

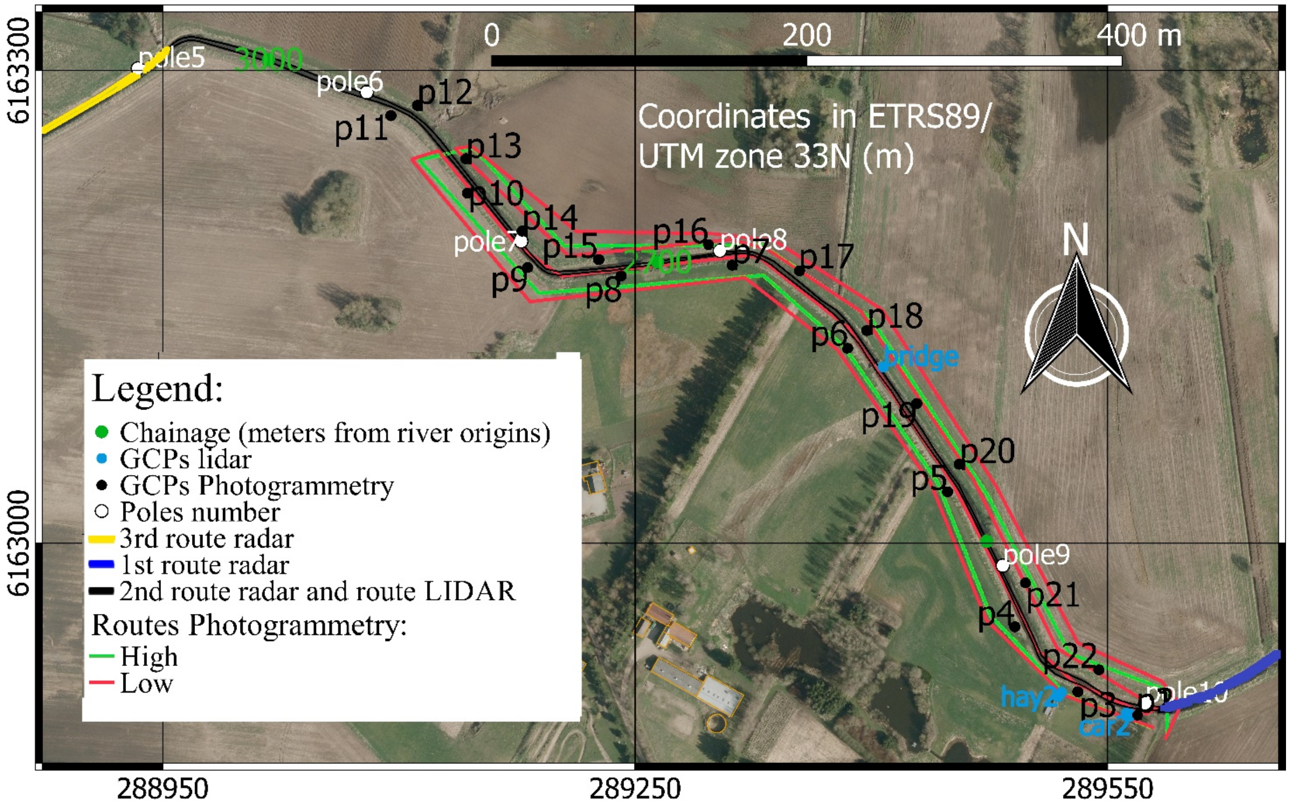

Fig. 3, map showing the flight route for photogrammetry and the Ground Control Points (GCPs) for photogrammetry for Åmose Å. The LIDAR route (equivalent to the 2nd route for radar) is also shown in this map together with GCPs for LIDAR. Map background is an orthophoto from the Danish Geodata Agency (Styrelsen for Dataforsyning og Effektivisering, 2018)

The radar observations were obtained along the entire ca. 2.3 km stretch, while observations for the LIDAR and photogrammetry were limited to a smaller stretch. A shorter stretch (ca. 0.9 km) was covered with photogrammetry because photogrammetry requires: i) multiple flight strips to monitor an area, and ii) GCPs. For this reason, photogrammetry is the most labour demanding technique. The total number of flights with LIDAR and photogrammetry was also limited by the need to obtain the UAS-borne and the in-situ ground-truth observations in a time lag of a few hours to avoid WSE fluctuation between the surveys. The maximum WSE variation was 1-2 cm during the survey, as measured by the gauging station shown in Fig. 2 (hydrometric data available online at Orbicon (2018)). The photogrammetry flight was conducted in daylight conditions to have sufficient illumination for optical imagery, while the LIDAR flight was conducted just after sunset, i.e. when the light conditions (absence of sunlight) were ideal for an active NIR sensor.

The radar flight paths consist of three consecutive routes (each route lasted ca. 12 minutes). For each route, the UAS is flown in a round trip (double-pass) along the river centreline.

The LIDAR path follows only one of the three radar routes (2nd route). The GCPs for LIDAR were used only as check points to evaluate the LIDAR accuracy, but GCPs are not used to directly georeference the LIDAR point cloud. These LIDAR GCPs consist of features clearly distinguishable with the LIDAR because of their elevation contrast with the surroundings. 7 LIDAR GCPs were chosen in total: 4 points on the roof of the car, 1 point on a small bridge crossing the stream and 2 points on flat hay bales.

The photogrammetry consists of two routes at different altitudes (30 and 70 meters above ground level). The camera was facing nadir for the route at 30 m. During the route at the highest altitude, the camera was facing nadir in one flight and it was tilted ca. 30° (from vertical, in a forward direction) in the other flight. Obtaining images at different altitudes and different angles ensured the highest accuracy in surfaces generation and DEM (e.g. Rossi et al., 2017; Wackrow and Chandler, 2011). 22 GCPs are used for photogrammetry (spatial distribution of GCPs is shown in Fig. 3, vertical variability range was ca. 1 m), of which 16 are directly used to geo-reference the model and 6 are check points to assess the absolute accuracy of the model.

Details about flight settings for each specific payload are given in Table 2.

2.2. Nivå case study

Fig. 4 shows a UAS-borne orthophoto map obtained with photogrammetric technique of the stream Nivå Å during the survey day. The river chainage is also shown in the figure.

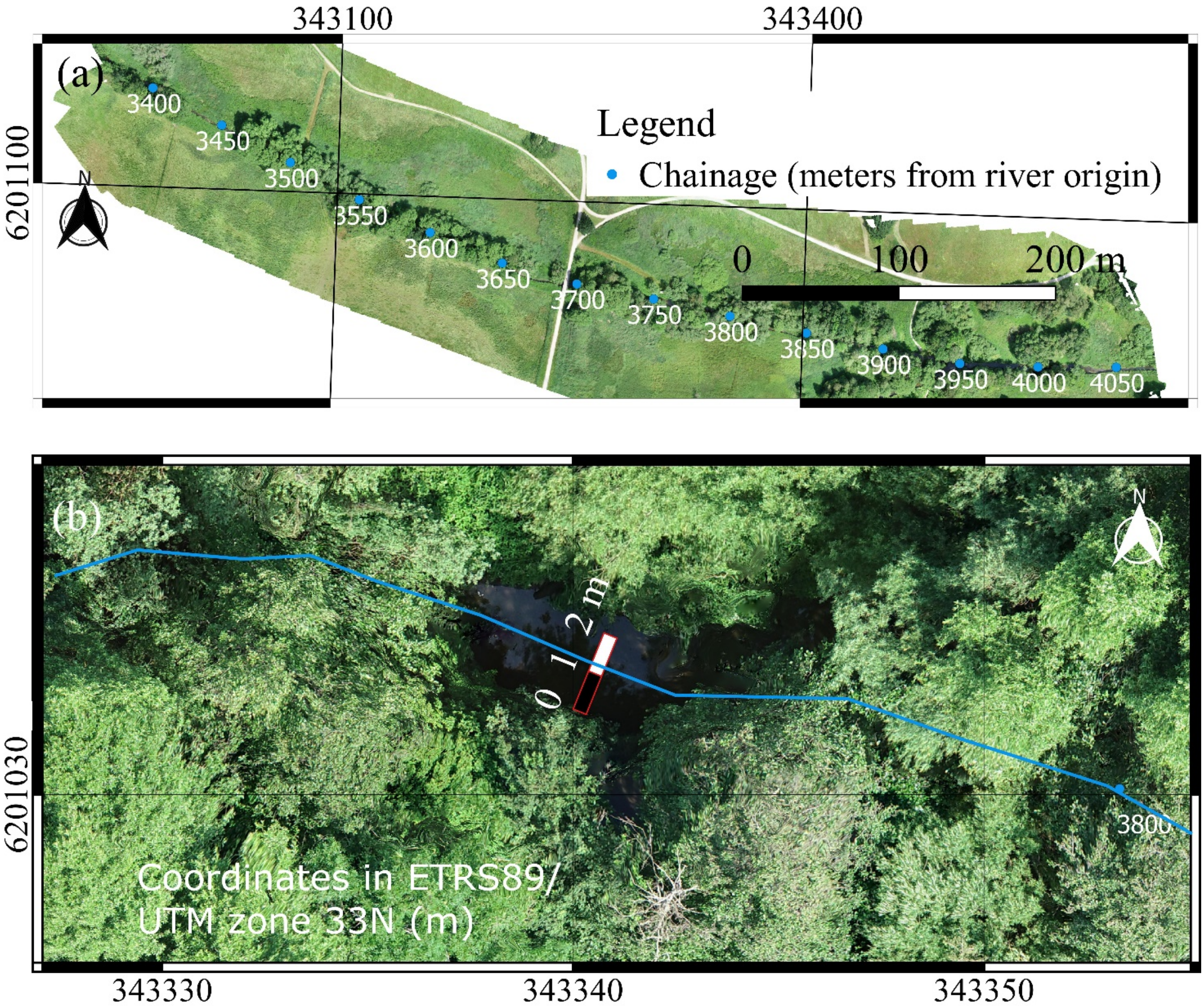

Fig. 4, UAS-borne orthopoto of Nivå Å. (a) Orthomap showing the river stretch that was surveyed for WSE. (b) detail of the stream. The stream has a width of 1-2 m at maximum. In most locations (in more than 90% of stretch length), the stream is fully covered by vegetation canopy.

The stream appears to be fully covered by dense canopy during the survey day, with WS that is visible on UAS-borne imagery only in sparse locations (less than 10% of the stretch length). This case study is a demonstration of the capabilities of the radar altimetry solution in environments where photogrammetry and LIDAR would fail to detect the WS because they would lack line-of-sight to the

WS. Also UAS navigation is complicated in this stream, indeed, the centerline is not clearly identifiable in the locations covered by vegetation, thus the UAS planned route can significantly differ (a few meters) from the river centerline.

2.3. Ground-truth observations

In-situ observations were obtained with the levelling technique (Fig. 5).

19 metal poles were installed along the surveyed stretch in Åmose Å and 4 poles were located along Nivå Å, in order to have stable in-situ reference points. The horizontal and vertical coordinates of these poles were measured on multiple days (one measurement every month during the period March-November 2018) with a GNSS rover station Trimble RTK GNSS R8s (Trimble Inc., USA).

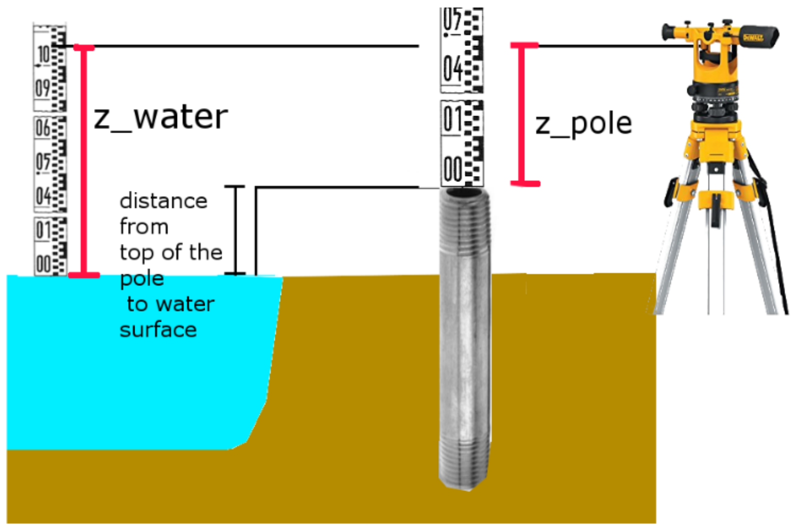

Fig. 5, levelling system for in-situ WSE ground-truth observations. Vertical absolute poles coordinates were measured with an RTK GNSS system.

The offset between the metal pole and the closest WS point was measured with the levelling instrument Leica Sprinter 50 Digital Level (Leica Geosystems, Switzerland). Levelling generally ensures sub-mm accuracy in height difference determination. However, the positioning of the measuring rod on the WS can generate an uncertainty of 1-2 cm, e.g. because of waves, ripples and operator errors. Furthermore, the absolute vertical coordinates of the poles were measured on different days to average the RTK GNSS errors, but an uncertainty of 1-2 cm is expected. Because of these sources of uncertainty, we can expect an accuracy of ground-truth in-situ observations of 2-3 cm.

2.4. UAS platforms and GNSS/IMU sensors

Observations with LIDAR and radar were retrieved with a DJI Matrice 600 PRO (DJI, China), as shown in Fig. 6, and imagery for the photogrammetry model was retrieved with a DJI Phantom 4 Pro (DJI, China).

Fig. 6, UAV flight to retrieve WSE observations in Åmose Å, Denmark.

The Matrice 600 Pro was equipped with the GNSS system OEM7700 (NovAtel, Canada) integrated through NovAtel's Synchronous Position, Attitude and Navigation (SPAN) technology with the IMU OEM-ADIS-16488 (Analog Devices, Inc., USA). To obtain cm-level accurate drone position, the GNSS (comprising GPS and GLONASS constellations) observations are post-processed with post-processed kinematic (PPK) technique with the software Inertial Explorer version 8.70 (NovAtel, Canada). A NovAtel Flexpack6 receiver with a NovAtel GPS-703-GGG pinwheel triple frequency (GPS and GLONASS) antenna was used as basestation. The IMU system was used to measure drone angles and processed with Inertial Explorer in a solution tightly coupled with the GNSS system, in order to filter GNSS observations and increase the position acquisition rate (Falco et al., 2017; Noureldin et al., 2013).

Observations of LIDAR and radar systems are saved and synchronized with GNSS and IMU observations on the single-board computer BeagleBone Black (BeagleBoard.org).

2.5. Radar

Bandini et al. (2017b) describe the UAS radar altimetry solution. As with satellite altimetry, the GNSS measures the altitude of the UAS above the reference ellipsoid (or sea level if geoid undulation is known), while the radar measures the range between UAS and the WS. By subtracting the range to WS from the GNSS-derived altitude, WSE can be determined. The accuracy in WSE estimates is a combination of the accuracy of both the ranging sensor and the GNSS system. The radar system used for this study is different from Bandini et al. (2017b). In this study, we adopted the Evaluation Module (IWR1443BOOST) of the IWR1443 radar chip from Texas Instrument (USA). The module costs ca. $300 (USD) and weighs ca. 50 g.

IWR1443 is a Frequency-Modulated Continuous-Wave (FMCW) radar chip capable of operating in the 76-81 GHz band with up to 4 GHz bandwidth continuous chirp (Texas Instruments, 2017). It is a fully configurable radar which supports 3 transmitting and 4 receiving antennas. Texas Instrument currently provides a mmWave Software Development Kit (SDK) for radar hardware and firmware configuration. The main advantage of this radar compared to the automotive radar used in Bandini et al. (2017b) is the possibility to obtain the full waveform of radar return. Appendix A reports the radar configuration parameters used for this research. This current configuration enables 2 receiving antennas and 1 transmitting antenna, 5 Hz frame rate (5 observations per second), 1024 range bins, and a range resolution of ca. 0.036 m. The radar field of view and the flight settings are given in Table 2, while details about radar configuration are given in Appendix A.

Fig. 7 shows the full waveform plot, obtained after applying a Fast Fourier transform (FFT) on the digitized samples corresponding to each chirp (Appendix A). The peak in each waveform is representative of the WS, because in the microwave spectrum WS has a higher reflectivity compared to soil and vegetation.

Analysing the waveform, a measuring accuracy value higher than range resolution can be achieved. Our experimental results, conducted in a laboratory with water tanks, showed that the optimal range value is obtained by extracting the range and power return of the maximum peak and of the previous and subsequent range bins, as according to experimental Eq. (1).

$$R = R_{peak} - \frac{res}{2} * \frac{pw_{peak} - pw_{next}}{(pw_{peak} - pw_{next}) + (pw_{peak} - pw_{previous})} + \frac{res}{2} * \frac{pw_{peak} - pw_{previous}}{(pw_{peak} - pw_{next}) + (pw_{peak} - pw_{previous})} = \quad (1)$$

$$R_{peak} + \frac{res}{2} * \frac{(pw_{next} - pw_{previous})}{2pw_{peak} - pw_{next} - pw_{previous}}$$

R is the range between the radar and the target (e.g. water surface), R_{peak} is the range corresponding to the range bin of the peak, res is the radar resolution (i.e. distance between two range bins, ca. 0.036 m in the current configuration), $pw_{peak}, pw_{previous}, pw_{next}$ are the return power (e.g. in

Decibels) of the range bin corresponding to the peak, the previous and the next range bin. In the equation, the range of the peak is adjusted by subtracting (in second term) and adding (in third term) a quantity equal to half the resolution multiplied by the difference between the peak return power and the return power of the next bin (in second term) or the previous bin (in third term), with each difference normalized by the sum of the two differences. Eq. (1) allows to estimate a range that was shown to be more accurate than extraction of just the range of the peak.

Laboratory experiments were performed under controlled conditions and the application of this formula has shown that a sub-centimetre accuracy can be obtained in range determination.

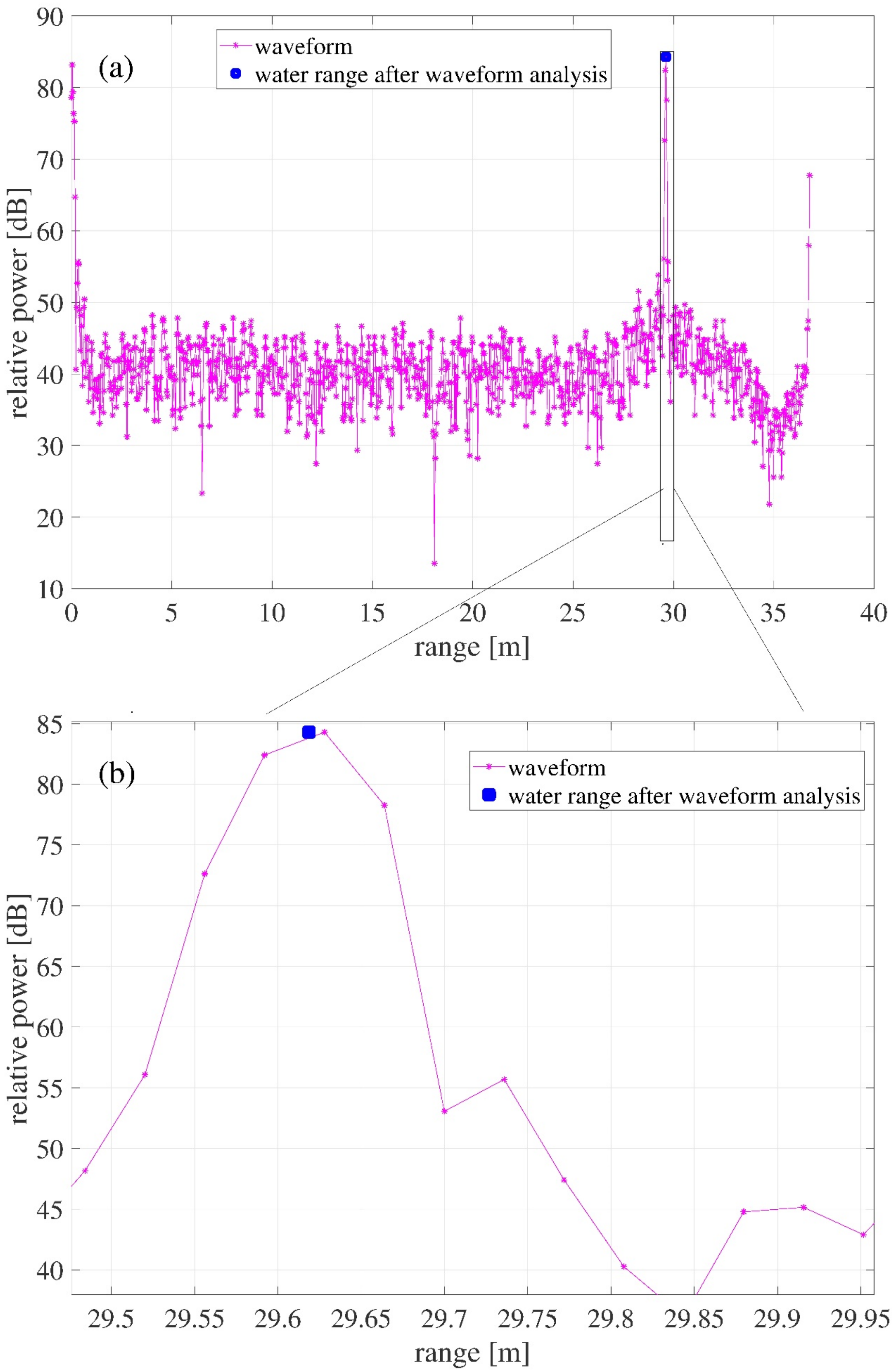

Fig. 7, waveform of a single radar observation above a river. (a) full waveform plot of the range bins of the radar (maximum range bin is ca. 36.78 m). The peak is representative of the WS. The *first and last bins show high returns but these are due to the direct wave and FFT numerical artefacts. (b) detail of the returns, highlighted by a black rectangle in (a), that are representative of the actual range to the water surface (estimated range to the WS is ca. 29.6186 m after applying Eq. (1)).*

The gimbal Gremsy T1 (Gremsy Co., Ltd, Vietnam) is currently used to stabilize and maintain the radar to a position facing nadir. The UAS-borne payload is shown in Fig. 8.

Fig. 8, UAS-borne radar. The current radar is stabilized through a gimbal. The gimbal is also equipped with an RGB camera for airborne pictures and videos.

The current UAS platform includes an accurate PPK GNSS system for post-processing UAS positions but does not include an RTK GNSS system for navigation. For this reason, UAS navigation showed to have a deviation of a couple of meters in both the vertical and the horizontal compared to the planned flight route. The UAS-radar altimetry observations include a few observations retrieved at locations where WS of this small stream was not visible to the radar antenna beam, because the UAS was not navigating above the stream but in the surroundings. These observations had to be filtered. In this study, this filtering is performed by including only radar observations that were captured when the UAS was positioned above the river mask, which was approximated using a polygon. This polygon was centred along the river centerline and its width (3 m Åmose and 1.5 m for Nivå) was chosen according to the stream size to approximate the river mask, for this reason we refer to this polygon as river polygon. Furthermore, altimetry observations were filtered to remove the few outliers (e.g. trees, bridges) that were at an elevation significantly different (more than 1 m) than WS. Another efficient option for filtering, which is not shown in this study, would be to determine a return power threshold to distinguish waveform peaks caused by land/trees/bridges from predominant peaks caused by the WS.

2.6. Photogrammetry

The UAS-imagery for the photogrammetry model was obtained with the CMOS RGB camera sensor (1 inch sensor, 20MP resolution) onboard Phantom 4 Pro. Camera settings for the flights are summarized in Table 2. UAS-imagery are processed in the software AgiSoft PhotoScan Professional (Version 1.4.5) retrieved from https://www.agisoft.com/.

We compared 3 different methods to estimate WSE from photogrammetry observations: i) extraction of elevation of the photogrammetric point cloud values contained in the river polygon (to be consistent with radar) ii) extraction of photogrammetric DEM elevation values along river centreline iii) extraction of the elevation of points at the “water-edge” to be consistent with the previously published methodology (Westaway et al., 2001, 2000; Woodget et al., 2015).

2.7. LIDAR

The LIDAR system is a Puck LITE™ (Velodyne LIDAR, US). It costed ca. $8,000 and weighs ca. 590 g. It provides dual return with a NIR wavelength of 903 nm. With 16 Channels, it is able to generate 300,000 points/second. Field of view and resolution are summarized in Table 2. Its typical accuracy over solid surfaces is ±3 cm: this accuracy corresponds to the accuracy of LIDAR only, without including GNSS or IMU errors.

LIDAR data are post-processed with the software LAStools (version 181119, academic), obtained from http://rapidlasso.com/LAStools. LAStools is used to visualize the point cloud, filter observations, and create the Digital Surface Model (DSM).

We found that the WS is not reflective enough to acquire direct LIDAR returns, so WSE cannot be directly measured. The main reason for this is probably the low energy that the LIDAR emits. This is a very common issue (e.g. Huang et al., 2018; Mandlburger et al., 2017) in the current lightweight LIDAR sensors (e.g. that can be deployed in small (less than 25 kg) UASs. Given this limitation in detecting the WS, LAStools needs to extrapolate from the “water-edge” points to construct a DEM of the stream.

We apply two methods to estimating WSE: i) extraction of all LIDAR point cloud elevation values contained in the river polygon (to be consistent with radar and photogrammetry) ii) extraction of the LIDAR DSM values along the river centreline.

379 *Table 2, platform, flight route and payload settings for the different sensors as used in this study*

Payload	Platform	Measurement rate	Altitude (above ground level)	Flight speed (m/s)	Image overlapping	Sensor orientation	Field of view (FOV) Resolution
Radar	DJI Matrice 600 PRO	5 Hz	28 m	3	-	Nadir	• Full waveform Estimated FOV at 77 GHz: • horizontal 3dB-beamwidth is ca. ±28° • elevation 3dB-beamwidth is ca. ±14°

Photogrammetry	DJI Phantom 4 Pro	3 sec between each image	30 m	2.5	*>80% frontal >60% side*	Nadir	• FOV: 84° • Ground Sample Distance (GSD) At 30 m: 0.9 cm/px, At 70 m: 2.10 cm/px
		3 sec between each image	*70 m*	*6*	*>80% frontal >60% side*	*Nadir*	
						30° (from vertical)	
LIDAR	DJI Matrice 600 PRO	300,000 points/second	28 m	3	-	Nadir	• FOV (Vertical): +15.0° to -15.0° • Angular Resolution (Vertical): 2.0° • FOV (Horizontal): 360° • Angular Resolution

							(Horizontal/Azimuth): 0.1° – 0.4°

3. Results

3.1. Radar

Fig. 9 shows the elevation bins obtained by subtracting the radar waveform from the GNSS altitude data. The colour map reflects the measured return power. The highest return power has an intense blue colour.

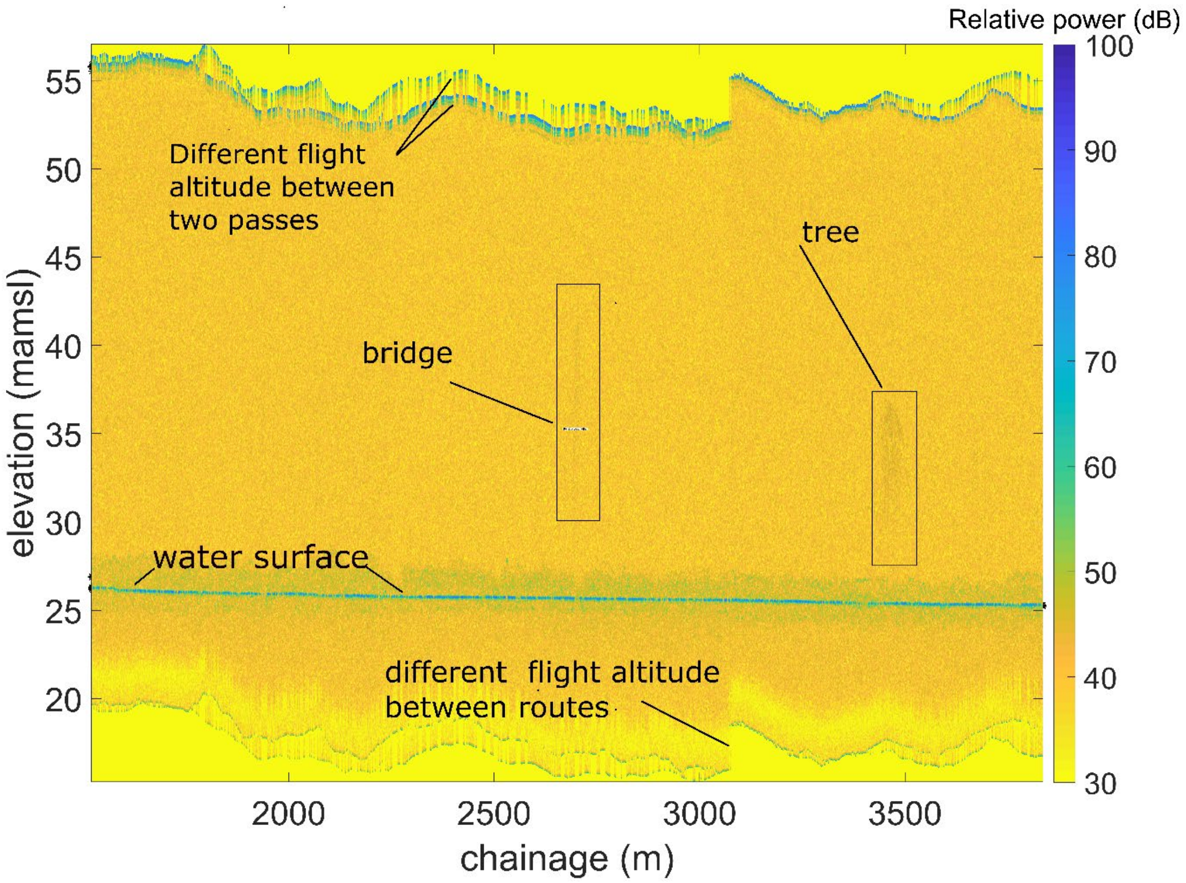

Fig. 9, colour map of the radar power returns of the flights above Åmose Å. X-axis shows river chainage, Y-axis shows the elevation bins (i.e. radar range bins subtracted from GNSS-derived altitude).

Fig. 9 depicts a clear WS profile, with a few outliers. The solid yellow colour at the bottom and top sides of the figure indicates elevation values that are above the flight altitude and below the minimum theoretical elevation bin, which is obtained by subtracting the maximum unambiguous range bin from the actual GNSS-derived altitude. The lowest and highest elevation bins vary depending on the flight altitude. The strong returns at the lowest and highest bins are not significant and can be generally ignored. Some of the outliers are caused by tree canopy or river structures above the WS (e.g. a bridge), as highlighted in the figure. Generally, trees with dense leaves cause a clear hyperbolic signal; however, at the time of the flight, trees were without leaves. Thus, the hyperbolic signal from trees is attenuated, with only perennial trees or large branches showing some returns predominant with respect to the WS.

WSE was extracted from the full waveform radar observations, as according to the waveform shape analysis technique described by Eq. (1).

Fig. 10 shows the in-situ ground-truth observations, the radar observations extracted from the waveform analysis and a spatial average of UAV observations at 5 m intervals.

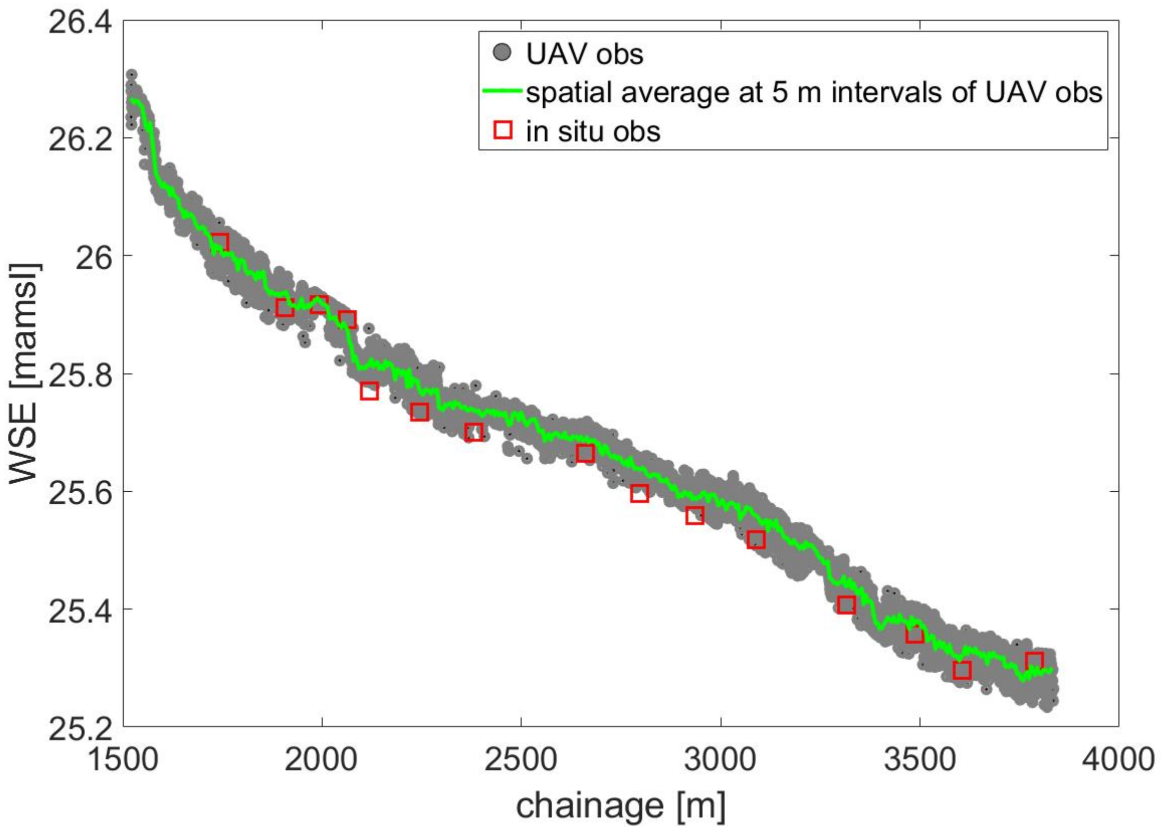

Fig. 10, WSE observations (in meters above mean sea level (mamsl)) retrieved by UAV-borne radar-GNSS technology and with in-situ levelling-RTK GNSS technique in Åmose Å. The size of the squares representing in-situ observations is arbitrary.

Fig. 10 shows that the radar solution is able to determine WSE with an accuracy better than 3 cm (Table 3 reports the statistics about error with comparison to ground-truth observations). This accuracy depends on two components: i) radar ranging accuracy and ii) vertical accuracy of the GNSS system.

3.2. Photogrammetry

Fig. 11 shows the orthophoto and the DEM model retrieved in the river stretch where photogrammetry was flown. Fig. 12 shows a detail (portion of the river stretch) of the orthophoto and DEM, with colour scale adapted to highlight the DEM estimation of WSE. The Ground Sample Distance (GSD) in final orthomosaic is ca. 2.1 cm/px.

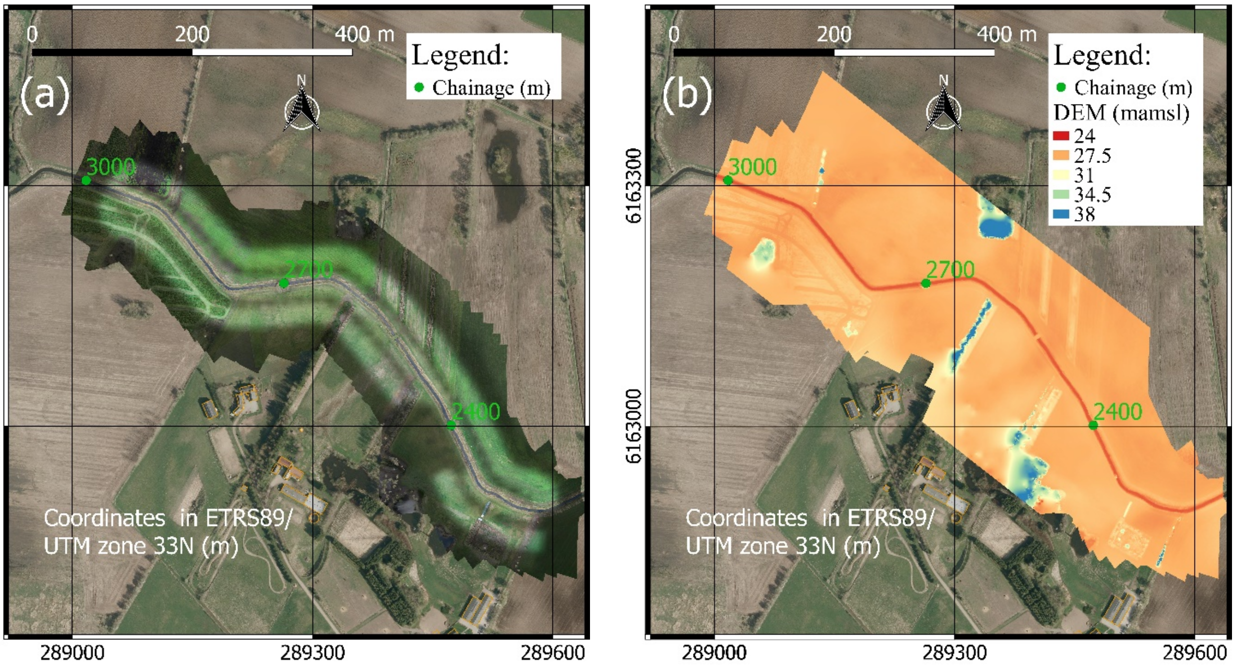

Fig. 11, Åmose Å: (a) shows the orthophoto, (b) shows the DEM computed with AgiSoft PhotoScan from the UAS-borne pictures.

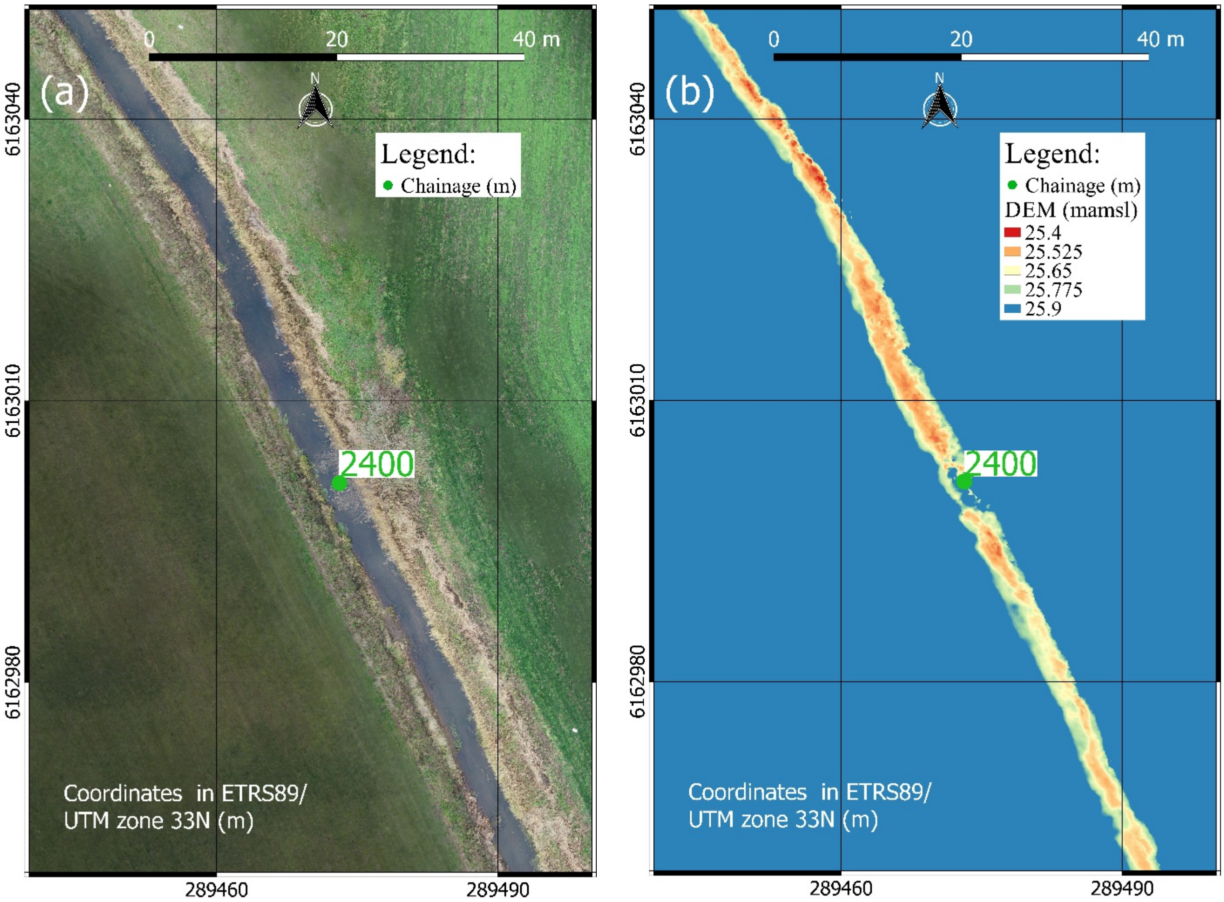

Fig. 12, Åmose Å: detail of (a) orthophoto and (b) DEM from UAS-photogrammetry

Fig. 13 shows a comparison of the WSE estimates of three different methods: i) cloud points values extracted inside the area contained by the river polygon, ii) DEM values extracted along centreline, iii) DEM values extracted along the "water-edge". Observations were filtered by removing the few outliers (e.g. trees, bridges) that were at an elevation significantly different (more than 1 m) from WSE and then subsequently removing observations below the 15th and above 85th percentile.

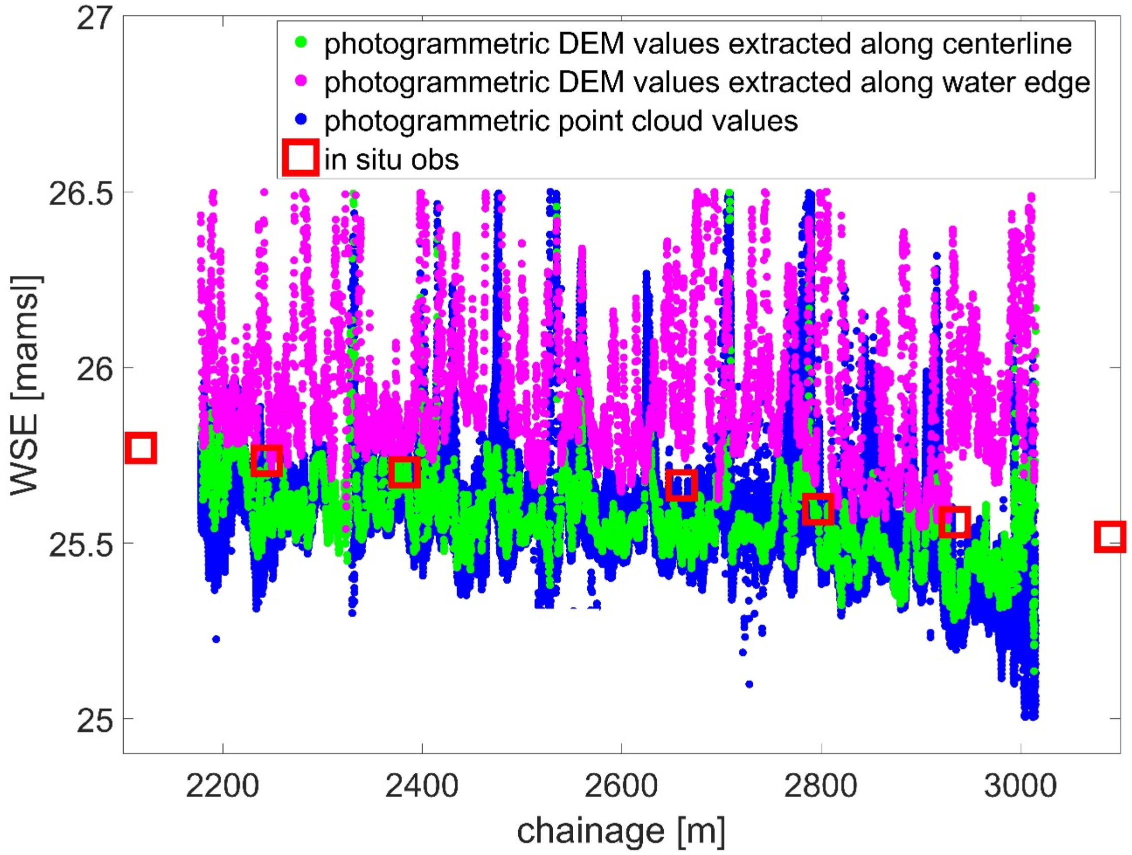

Fig. 13. Photogrammetry in Åmose Å: comparison of the elevation of the point cloud in the river polygon with the DEM values extracted along centerline and along the edge.

Fig. 13 shows peaks that are caused by the trees and the bridge. The point cloud shows the larger standard deviation, with the DEM centrelines values and the DEM “water-edge” having lower dispersion. The “water-edge” values are at a higher elevation compared to the other two datasets, this is mainly due to the streambank grass protruding over the stream and affecting the “water-edge” elevation.

3.3. LIDAR

The LIDAR instrument was not directly able to detect the WS. Even at nadir, where we expect the highest reflection from the WS (Hopkinson et al., 2011), WS returns were not acquired by the instrument.

Fig. 14 shows that the point cloud includes observations in the stream area only in the patches where surface vegetation plants are present.

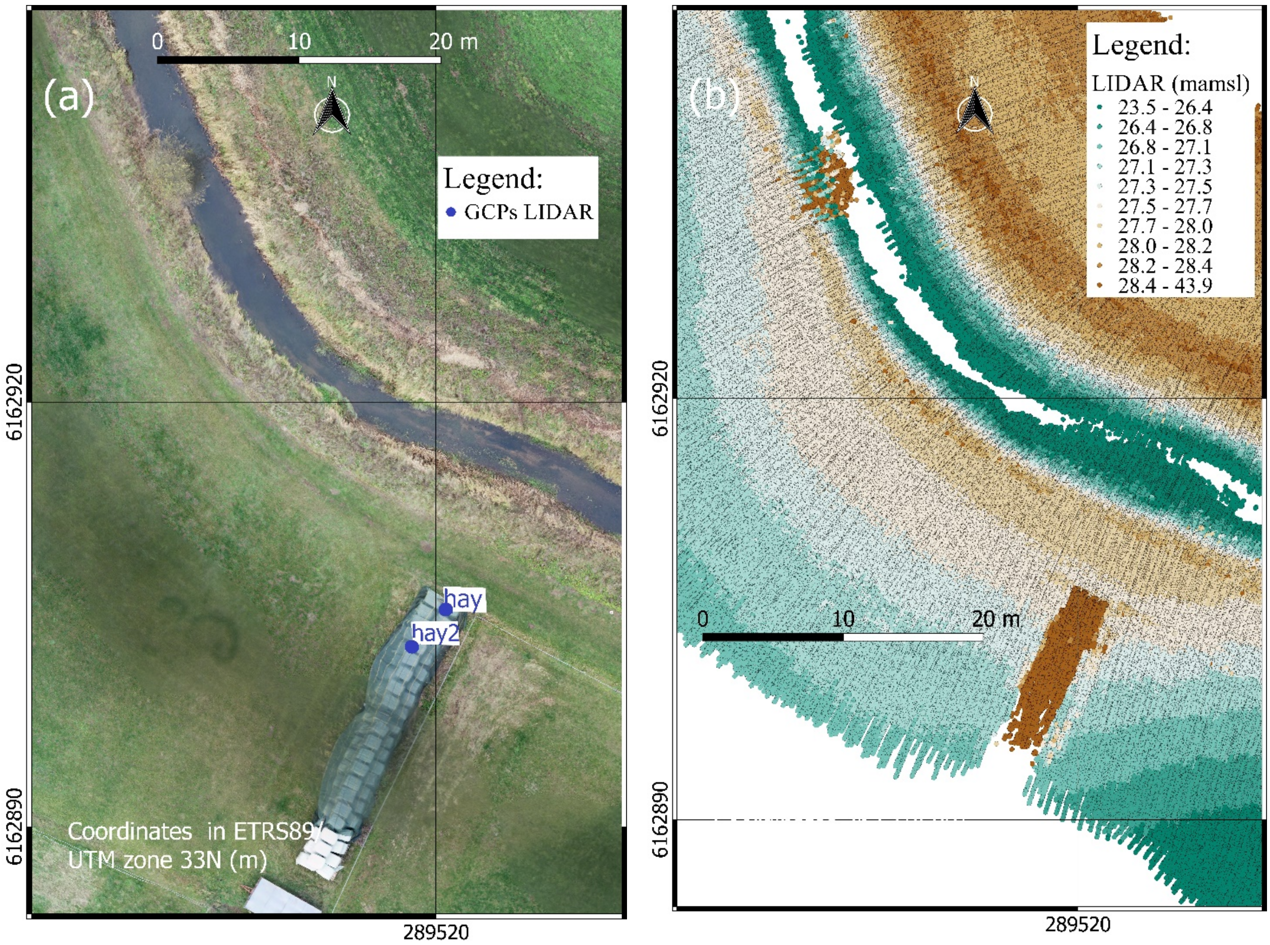

Fig. 14, Åmose Å: detail of photogrammetry and LIDAR point cloud in a stream portion. (a) shows the orthophoto obtained in the same location as (b), which is the LIDAR point cloud.

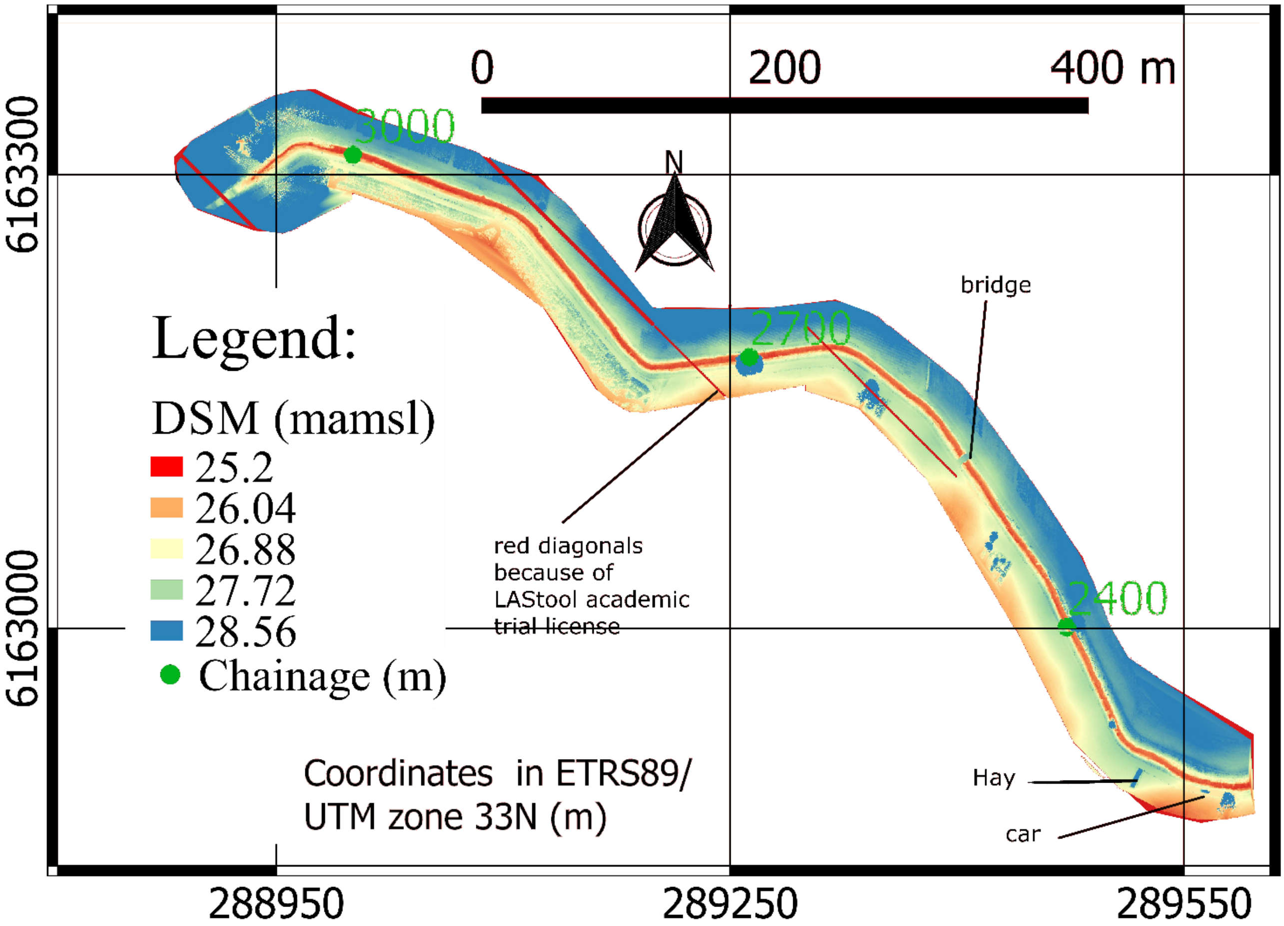

Fig. 15, Åmose Å: DSM obtained from LIDAR point cloud. The red diagonals are caused by the academic trial license of LAStool.

Because the LIDAR could not acquire sufficient reflection from the WS and the DSM shown in Fig. 15 is estimated by the software LAStools mainly by extrapolating the observations obtained at the streambank points.

Fig. 16 shows the LIDAR observations extracted i) along the river centerline from the DSM and ii) from the point cloud contained in the river polygon. Similarly to photogrammetry, LIDAR observations were filtered by altimetry observations were filtered to remove the few outliers (e.g.

trees, bridges) that were at an elevation significantly different (more than 1 m) from WSE and then subsequently removing observations below the 15th and above the 85th percentile.

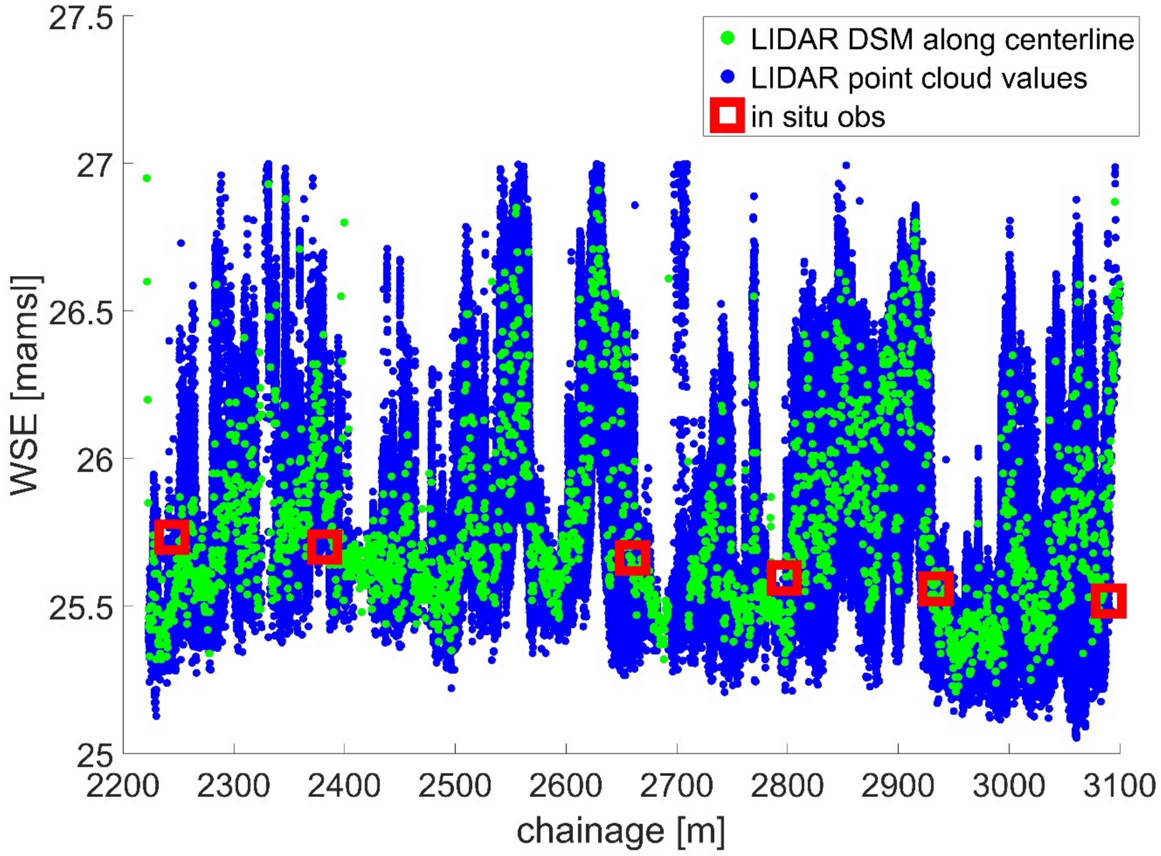

Fig. 16, Åmose Å: comparison of different methods to extract WS from LIDAR DSM and point cloud.

As shown in Fig. 16, the LIDAR observations show large standard deviation: trees and the bridge overhanging the stream induce the most evident peaks, but also in areas where there are no overhanging trees the observations show large dispersion. This is mainly due to the fact that the WS is not reflective enough. Therefore, the LIDAR does not directly acquire WS returns, but instead mainly retrieves observations of aquatic surface plants and of streambank grass that protrudes over the stream.

3.4. Comparing radar altimetry, photogrammetry and LIDAR

Check point to evaluate measurement accuracy of land elevation

The accuracy of the photogrammetric DEM on estimating land elevation is evaluated on the 16 GCPs directly used in the geo-referencing process and on the 6 check points. A vertical RMSE of less than 2.5 cm and a horizontal RMSE of 2 cm are estimated by AgiSoft PhotoScan on the geo-referencing GCPs, while a vertical RMSE of 3 cm and a horizontal RMSE of 2.5 cm are computed on the check points. Therefore, the photogrammetric DEM could estimate land elevation with an RMSE generally better than 3 cm.

The LIDAR accuracy in land elevation estimates was lower: an RMSE of 30 cm on the horizontal and 15 cm on the vertical were estimated when comparing the LIDAR designated GCPs. This large LIDAR error is mainly due to the inaccuracy in the IMU estimates, especially on the azimuth angle, and on the uncertainty in determining the angle offset between the IMU and the LIDAR reference planes. A horizontal angle uncertainty of 1-2 degrees can result in large horizontal errors in the LIDAR DSM. This could be improved in the future by using a system with 2 GNSS antennas to provide accurate heading and improve the a priori knowledge of the angle offsets between the IMU system and the LIDAR reference planes.

The radar system is not developed to monitor land elevation, thus the accuracy of the radar in land elevation measurements was not assessed.

WSE estimates

Fig. 17 compares the LIDAR, photogrammetry and radar observations extracted from the point cloud contained in the river polygon.

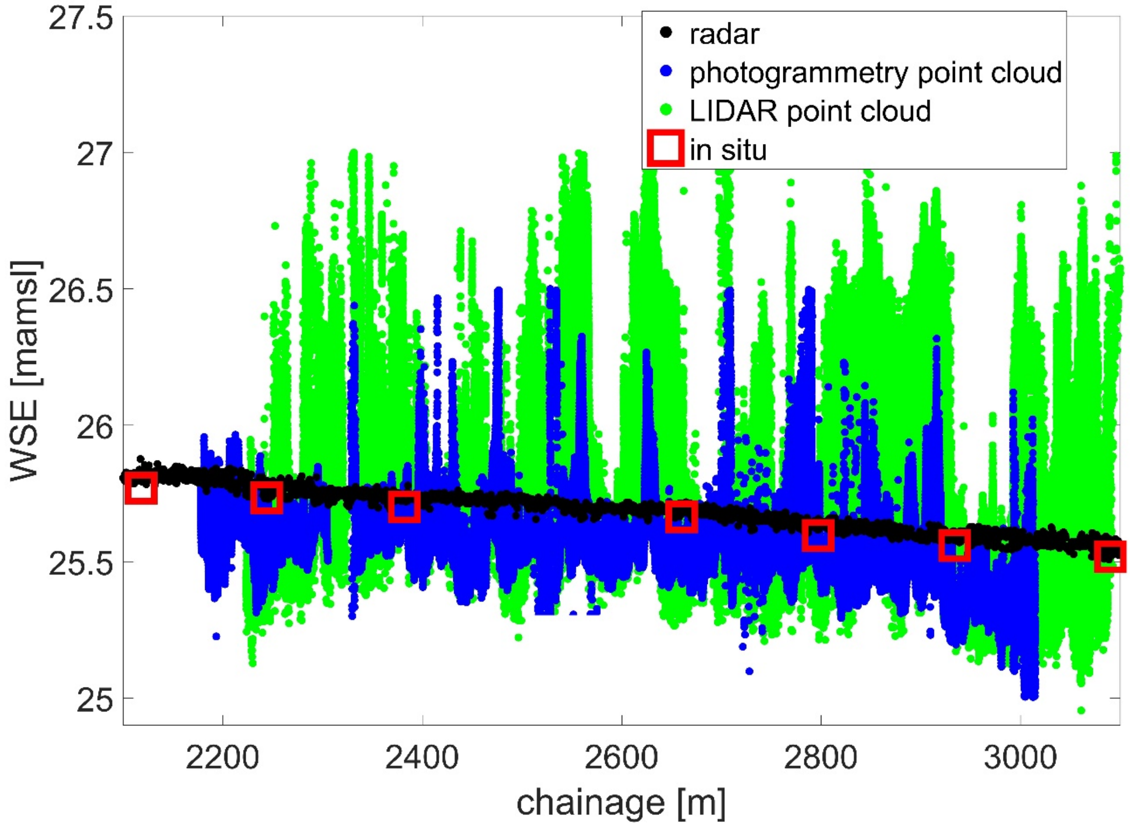

Fig. 17. Åmose Å: Comparison of radar, photogrammetry and LIDAR elevation values extracted in the point clouds.

Table 3 shows a comparison of the accuracy and standard deviation of the 3 different techniques in WSE determination.

Table 3, statistics showing measurement standard deviation and accuracy of the different UAV-borne technology when compared to in-situ measurements in Åmose Å. Average Standard deviation (σ) is computed by averaging the standard deviation of the 5 meters intervals in which the stream reach (~2.3 km) was discretized. Mean Absolute Error (MAE), Mean Bias Error (MBE), Root Mean Square Error (RMSE) were computed by comparing the in-situ observations with the average of UAV observations obtained at intervals of 5 m, i.e. 2.5 m before and 2.5 m after the in-situ measurement location. Lidar and photogrammetry were compared with the ground-truth observations in the 800 m stretch that is covered by both Lidar and photogrammetry flights, radar statistics are shown both for the 2.3 km stretch and for the 800 m stretch in common with Lidar and photogrammetry.

Technology	σ (m)	MAE (m)	MBE (m)	RMSE (m)

Radar (2.3 km stretch- 19 ground-truth observations)	0.014	0.029	0.019	0.031
Radar (800 m stretch, only ground-truth observations in common with LIDAR and photogrammetry)	0.012	0.033	0.033	0.03
Photogrammetry DEM centerline	0.048	0.15	-0.151	0.164
Photogrammetry DEM "water-edge"	0.106	0.385	0.385	0.450
Photogrammetry Point cloud	0.073	0.160	-0.160	0.180
LIDAR DSM centerline	0.120	0.238	0.076	0.358
LIDAR point cloud	0.15	0.159	0.033	0.2218

Table 3 shows that the radar observations have a standard deviation and accuracy that are approximately one order of magnitude higher than LIDAR or photogrammetry.

In this specific study, the "water-edge" method for photogrammetry showed higher values for the error metrics compared to the extraction of observations from both the river centerline and the point cloud contained in the river polygon. The extraction of LIDAR values from the point cloud values shows values for the error metrics relatively similar to the LIDAR centerline technique: this is because the LIDAR does not obtain any return from the WS and LAStools software needs to extrapolate observations from the edges to create the DEM in the stream area. These results suggest that the current LIDAR and photogrammetry methods do not provide an accuracy below the decimetre level in a stream with streambank vegetation (e.g. herbaceous plants) that affects the water-edge detection.

3.5. Result-Nivå Å survey

Fig. 18 shows the full waveform of the radar for Nivå Å. The stream appears to be fully covered by tree canopy (blue "shadows" are the hyperbolic signatures of the tree canopy). However, a high return power signal clearly depicts the WS in the colour plot. The WS signal is lost where the UAS navigation fails to accurately follow the river course, especially where the stream is very narrow and the canopy very dense.

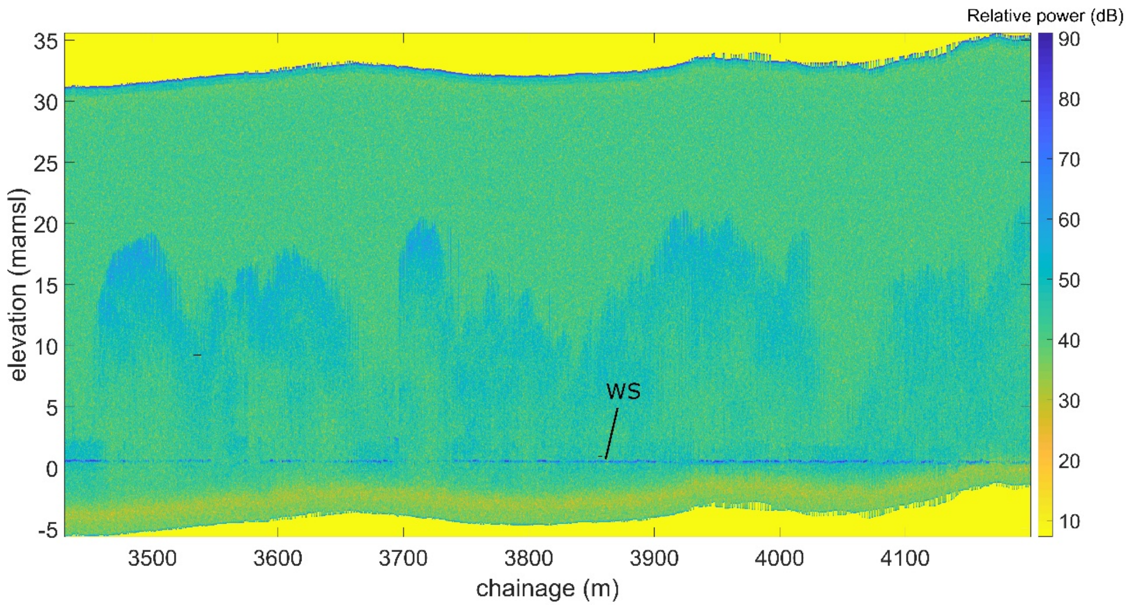

Fig. 18, radar full waveform in Nivå Å. Blue shadows are the hyperbolic signatures of trees.

WS was extracted from the return peak of each waveform, as shown in Fig. 19, and compared with ground-truth observations.

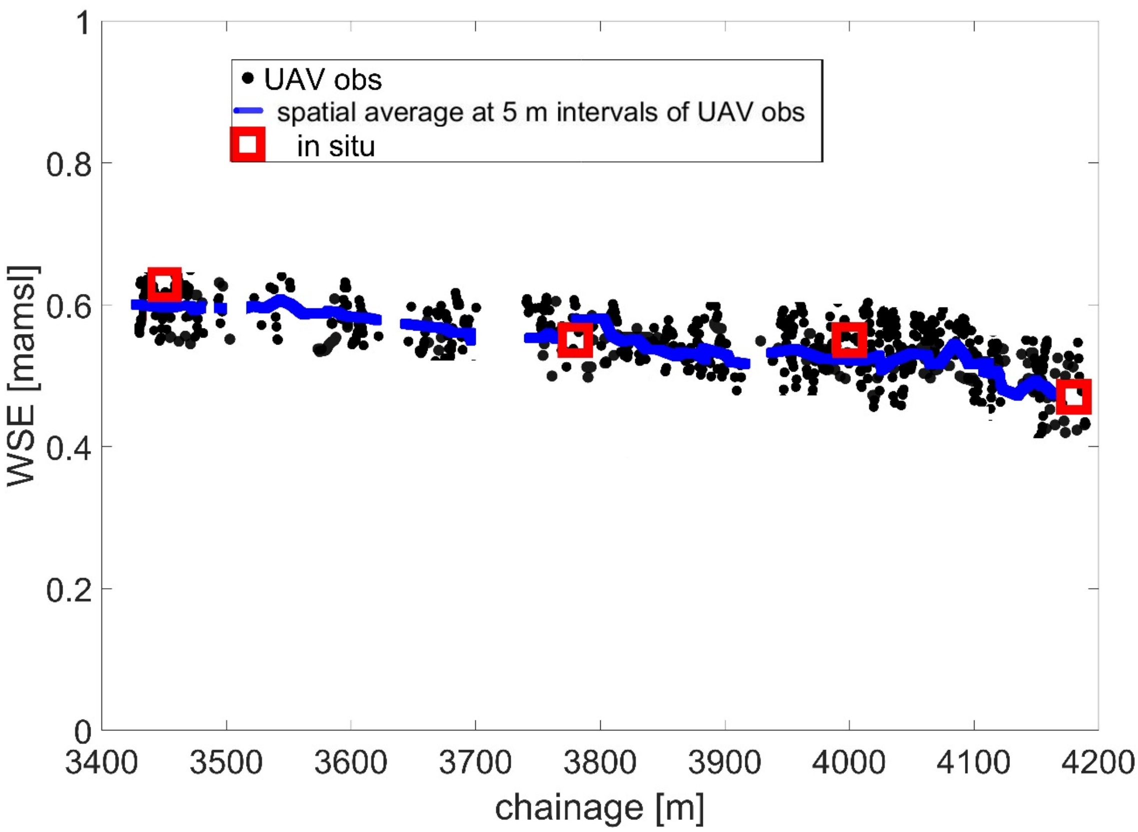

Fig. 19, WSE observations (in meters above mean sea level (mamsl)) retrieved by UAV-borne radar-GNSS technology and with ground-truth levelling-RTK GNSS technique in Nivå Å. The size of the squares representing ground-truth observations is arbitrary.

Fig. 19 shows that the radar retrieved observations also in this challenging environment, with very narrow stream covered by vegetation. Only in few areas, the radar failed to capture observations of the stream WSE.

The RMSE of the observations showed a MBE of 1.7 cm, a MAE of 3 cm, a RMSE of ca. 3.2 cm and an average standard deviation, computed by averaging the standard deviation of the 5 meters intervals, of ca. 2.4 cm.

4. Discussion

We demonstrated that UAS platforms can retrieve highly accurate WSE observations. UAS ensure a spatial resolution higher than spaceborne or airborne remote sensing technique, with a spatial coverage and survey time significantly lower than ground-truth techniques. A few days of field work are needed for retrieving WSE, at the same accuracy and same spatial resolution level as UAS-radar altimetry observations, with in-situ instrumentations (e.g. with RTK-GNSS systems, levelling systems or terrestrial laser scanners). Furthermore, GNSS floaters or remotely operated aquatic vehicles are not practical autonomous solutions in densely vegetated streams and cannot retrieve WSE observations at the same accuracy level as UAS-radar altimetry. Indeed, in small rivers with dense aquatic and riparian vegetation, GNSS antennas positioned at the WS level do not have a clear sky view, furthermore, signal multipath caused by the WS and by the surroundings reduces the GNSS accuracy.

Table 4 compares the estimated market price of the three different UAS-borne WSE measuring techniques: radar, LIDAR and photogrammetry.

Table 4, comparison of the market price of the different UAS-borne techniques to measure WSE

Technique	**Cost of the UAS-borne payload (US dollars)**	**Weight**	**Deployed UAS Platform**	**GCPs required**	**Time to survey 1 km stretch**	**Time to process 1 km stretch**
Radar	Radar: ca. \$300 Gimbal: ca. \$300-2000 PPK/RTK GNSS+IMU: \$1000-10000	Radar: 0.05 kg Gimbal: 0.5-1.5 kg PPK/RTK GNSS+IMU: ca. 0.15-0.4 kg	DJI Matrice 600 Pro[1]	NO	ca. 10 minutes	ca. 10 minutes

			Ca. $6400			
LIDAR	LIDAR: ca. $8000 PPK/RTK GNSS+IMU: $1000-10000	LIDAR: ca. 0.6 kg PPK/RTK GNSS+IMU: ca. 0.15-0.4 kg	DJI Matrice 600 PRO Ca. $6400	NO	ca. 10 minutes	A few hours
Photogrammetry	RGB Camera: $400-5000 Gimbal: $300-2000 GNSS+IMU: $300-10000	Camera+gimbal: 0.1-3 kg GNSS+IMU: ca. 0.1-0.4 kg	DJI Phantom 4 Pro $2000 (includes GNSS and IMU)	Generally required	30-120 minutes	A few days

[1]A smaller and cheaper UAS platform could potentially be used.

Table 4 shows that in terms of price, the radar sensor is the most competitive. However, this solution requires a GNSS rover receiver (preferably dual frequency) on the UAS and a base station (i.e. differential GNSS system with either PPK or RTK processing), which should be included in the cost. Furthermore, the radar solution could also include an IMU, which may be integrated to the GNSS to improve the position solution or could be used to retrieve the UAS angles when the radar is not stabilized with a gimbal. In case GCPs are used, the photogrammetry solution does not require a dual frequency GNSS receiver and a base station, i.e. low-cost GNSS could be used for photogrammetry. Only if direct geo-referencing (Carbonneau and Dietrich, 2017; Cramer et al., 2000; Rehak et al., 2013; Turner et al., 2014) was adopted, GCPs could be reduced or theoretically avoided, but in this case the UAS would require: i) accurate GNSS receivers and IMU sensors (similar to the ones deployed in our radar payload) that should be accurately synchronized with the camera solution ii) high-accuracy calibration of the UAS camera.

The radar and LIDAR sensors show the shortest survey time. Differently, UAS-photogrammetry requires longer flight time: multiples flight strips to acquire images at different angles and flight routes at different altitudes and with different camera angles should be performed.

For the radar, processing time is short (in the orders of few minutes with consumer grade laptops). The post-processing of radar observations is already automatized, with most of the human-computer interaction (generally a few minutes) that needs to be spent to import and process GNSS radar in the GNSS processing software. LIDAR has shown longer processing time because of the high point density, with human-computer interaction required to filter observations according to river mask and create DSM and DTM. Photogrammetry is the most demanding application in terms of computational times. A few days are normally required to process the high resolution RGB images also with the current optimized computer server, which consists of AMD Ryzen Threadripper 1950X processor with 16 cores, 3400 Mhz with two graphic cards (Nvidia GeForce GTX 1080). Furthermore, the processing time is not deterministic and varies depending on the image match points that are identified by the software. Significant human-computer interaction time is required to identify the “water-edge” and to extract WSE observations along this “water-edge”.

The accuracy of UAS-borne radar WSE does not depend on water depth and water turbidity. Furthermore, as shown in this study, UAS-borne WSE can be retrieved also in small stream covered by dense vegetation canopy. This is a clear advantage compared to WSE measurements with UAS-borne lidar and photogrammetry, which are effected by water turbidity, water depth (e.g. a visible riverbed or aquatic vegetation in the imagery can complicate construction of the WSE photogrammetric model) and require line-of-sight with the WS, which is limited in case of dense vegetation overhanging the stream.

UAS-WSE observations represent a new dataset in hydrology: radar altimetry can capture WSE profiles, in agreement with the 1-D WSE simulation of most of the hydrodynamic river models (e.g.

MIKE 11, HEC-RAS, etc.). In case of large rivers or floodplains, multiple flight routes can be easily conducted to measure the WSE at different points across the river. Accurate WSE slope measurements can improve understanding of how spatial irregularities in river bathymetry affect river hydraulics (Garambois et al., 2017), enhance knowledge about surface water-groundwater interaction processes (Bandini et al., 2017a; Pai et al., 2017) and resolve channel roughness with high spatial resolution (Schneider et al., 2018).

WSE can be retrieved autonomously during extreme events (e.g. floods) with our radar altimetry solution, without any GCP and without sunlight. Indeed, radar is not affected by light conditions, while e.g. photogrammetry relies on sunlight. Regarding the current UAS-platform, the main limitation is the weather condition during an extreme event: the UAS platforms deployed in this study can withstand a wind of at least 8-10 m/s but can fly only in light rain conditions.

Furthermore, discharge could be better estimated with UAS-borne observations, e.g. by informing Manning's equation or hydrodynamic models with WSE slope measurements and by deriving rating curves (e.g. Bjerklie et al., 2005; LeFavour and Alsdorf, 2005; Tarpanelli et al., 2013).

WSE measurements in combination with discharge (Q) can be used to construct rating curves, which are essential for estimating discharge based on real-time WSE measurements. Discharge computation requires wetted area (Ω) and mean flow velocity (V), which are usually measured with in-situ surveys that are generally time-consuming and labour intensive, especially in large rivers during extreme conditions. Manfreda (2018) describes an approach to express V and Ω both as a function of WSE and river bed geometry.

5. Conclusions

We compare the WSE estimates from 3 different UAS-borne methods: LIDAR, photogrammetry and an innovative radar altimetry solution:

- The radar altimetry solution with full waveform analysis shows the best accuracy in WSE estimates, with RMSE ca. 3 cm and σ ca. 1.5 cm, while photogrammetry and LIDAR show an RMSE and σ of decimetres.
- The LIDAR and the radar solution do not require GCPs and allow for single-pass routes, while photogrammetry requires longer survey times because it requires GCPs and multiple flight strips.
- The developed radar solution requires significantly shorter computational and human-computer interaction time. The computational time that is required to process observations of a 1 km stretch is in the order of minutes for radar, hours for LIDARs, days for photogrammetry.
- The main advantage of the LIDAR and photogrammetry compared to radar is the capability of producing a DEM of the riverbank topography, while radar can only determine the WSE and its slope.

In our view, UAV-borne WSE observations can be defined as a new datatype in river hydrology: i) compared to other remote sensing techniques they ensure high accuracy and can be acquired also in the smallest vegetated streams ii) compared to in-situ measurements they ensure high spatial resolution and higher spatial coverage at lower cost. UAV-borne WSE observations can significantly improve flood forecast models, improve our knowledge about the effect of river geometry and hydraulic roughness on WSE and contribute to construction of rating curves.

Acknowledgments

We thank Karsten Stæhr Hansens from Orbicon A/S for having retrieved the in-situ ground-truth observations. The choice of having in-situ observations acquired by a professional operator from Orbicon engineering company was motivated with the need to perform an independent accuracy validation test of the radar WSE observations.

Funding

This work was partly funded within the RIVERSCAPES project by the Innovation Fund Denmark under file number 7048-00001B.

Code and data availability.

Datasets used in the study are available online in the repository archived in Zenodo.org (http://doi.org/10.5281/zenodo.3519888). The repository contains UAS-borne observational datasets and programming scripts to analyze data.

Appendix A

The report from Dham (2017) provides a short overview on the chirp timing parameters that are needed to configure an FMCW radar, as shown in Fig. A1.

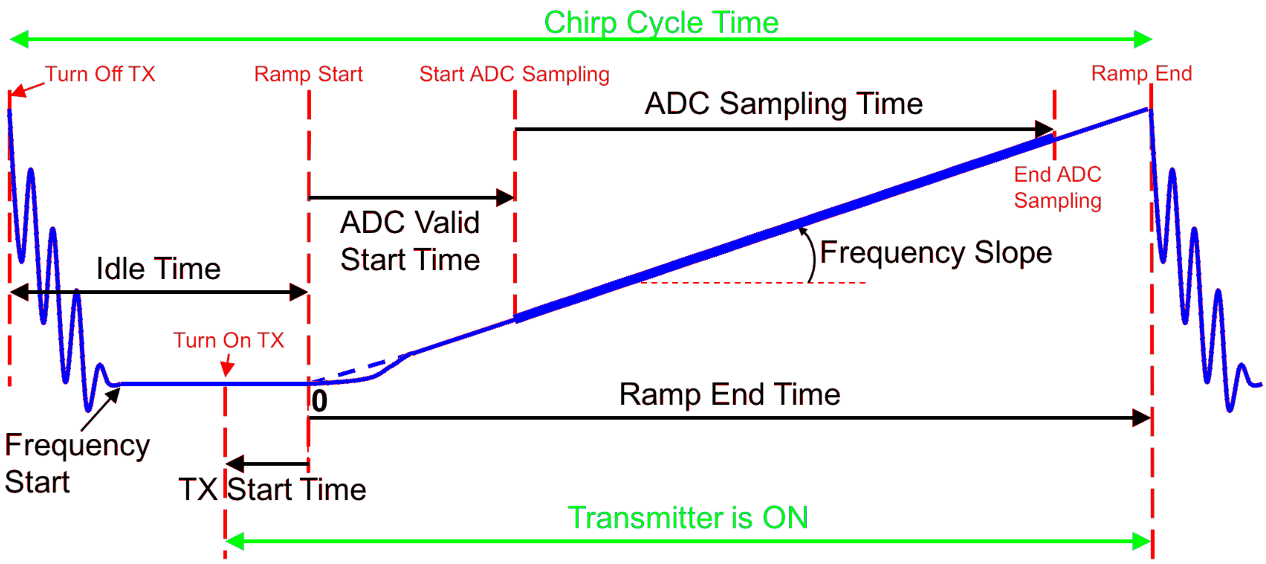

Fig. A1, chirp configuration, Source: Dham, Texas Instrument (2017)

An FMCW radar typically sends out a sequence of chirps (i.e. a sinusoid whose frequency increases linearly with time), equally spaced in time, in a unit called a frame (Rao, 2017).

Table A1, chirp parameters chosen for the radar configuration

Chirp timing parameters	Parameter value
ADC Sampling Rate	8.580 millions of sample per seconds
ADC sampling time	106.29 µs
number of ADC samples collected during ADC sampling time	912
frequency slope	35 MHz/ µs
frequency start	77 GHz
ramp end time	114.3 µs
ADC valid start time	7 µs
Idle time	2929 µs

The radar was configured with 1 transmitting antenna and 2 receiving antennas, with the chosen chirp configuration resulting in a bandwidth of 4 GHz, a measurements rate of 5 Hz, maximum unambiguous range of ca. 30 m, and vertical resolution of ca. 0.036 m. Table A1 shows the specific radar configuration parameters. The specific configuration parameters are shown in Table A1.

Reference list

Allouis, T., Bailly, J.S., Pastol, Y., Le Roux, C., 2010. Comparison of LiDAR waveform processing methods for very shallow water bathymetry using Raman, near-infrared and green signals. Earth Surf. Process. Landforms 35, 640–650. https://doi.org/10.1002/esp.1959

Alsdorf, D.E., Rodriguez, E., Lettenmaier, D.P., 2007. Measuring surface water from space. Rev. Geophys. 45, 1–24. https://doi.org/10.1029/2006RG000197

Altenau, E.H., Pavelsky, T.M., Moller, D., Lion, C., Pitcher, L.H., Allen, G.H., Bates, P.D., Calmant, S., Durand, M., Smith, L.C., 2017. AirSWOT measurements of river water surface elevation and slope: Tanana River, AK. Geophys. Res. Lett. https://doi.org/10.1002/2016GL071577

Andersen, M.S., Gergely, Á., Al-Hamdani, Z., Steinbacher, F., Larsen, L.R., Ernstsen, V.B., 2017. Processing and performance of topobathymetric lidar data for geomorphometric and morphological classification in a high-energy tidal environment. Hydrol. Earth Syst. Sci. https://doi.org/10.5194/hess-21-43-2017

Asadzadeh Jarihani, A., Callow, J.N., Johansen, K., Gouweleeuw, B., 2013. Evaluation of multiple satellite altimetry data for studying inland water bodies and river floods. J. Hydrol. 505, 78–90. https://doi.org/10.1016/j.jhydrol.2013.09.010

Bandini, F., Butts, M., Jacobsen, T.V., Bauer-Gottwein, P., 2017a. Water level observations from unmanned aerial vehicles for improving estimates of surface water-groundwater interaction. Hydrol. Process. https://doi.org/10.1002/hyp.11366

Bandini, F., Jakobsen, J., Olesen, D., Reyna-Gutierrez, J.A., Bauer-Gottwein, P., 2017b. Measuring water level in rivers and lakes from lightweight Unmanned Aerial Vehicles. J. Hydrol. 548, 237–250. https://doi.org/10.1016/j.jhydrol.2017.02.038

Biancamaria, S., Frappart, F., Leleu, A.S., Marieu, V., Blumstein, D., Desjonqueres, J.D., Boy, F., Sottolichio, A., Valle-Levinson, A., 2017. Satellite radar altimetry water elevations performance over a 200 m wide river: Evaluation over the Garonne River. Adv. Sp. Res. 59, 128–146. https://doi.org/10.1016/j.asr.2016.10.008

Biancamaria, S., Lettenmaier, D.P., Pavelsky, T.M., 2016. The SWOT Mission and Its Capabilities for Land Hydrology. Surv. Geophys. https://doi.org/10.1007/s10712-015-9346-y

Bjerklie, D.M., Moller, D., Smith, L.C., Dingman, S.L., 2005. Estimating discharge in rivers using remotely sensed hydraulic information. J. Hydrol. 309, 191–209. https://doi.org/10.1016/j.jhydrol.2004.11.022

Blume, T., van Meerveld, I., Weiler, M., 2017. The role of experimental work in hydrological sciences–insights from a community survey. Hydrol. Sci. J. https://doi.org/10.1080/02626667.2016.1230675

Brzank, A., Heipke, C., Goepfert, J., Soergel, U., 2008. Aspects of generating precise digital terrain models in the Wadden Sea from lidar-water classification and structure line extraction. ISPRS J. Photogramm. Remote Sens. https://doi.org/10.1016/j.isprsjprs.2008.02.002

Bühler, Y., Adams, M.S., Stoffel, A., Boesch, R., 2017. Photogrammetric reconstruction of homogenous snow surfaces in alpine terrain applying near-infrared UAS imagery. Int. J. Remote Sens. https://doi.org/10.1080/01431161.2016.1275060

Calmant, S., Seyler, F., 2006. Continental surface waters from satellite altimetry. Comptes Rendus - Geosci. 338, 1113–1122. https://doi.org/10.1016/j.crte.2006.05.012

Canny, J., 1986. A Computational Approach to Edge Detection. IEEE Trans. Pattern Anal. Mach. Intell. https://doi.org/10.1109/TPAMI.1986.4767851

Carbonneau, P.E., Dietrich, J.T., 2017. Cost-effective non-metric photogrammetry from consumer-grade sUAS: implications for direct georeferencing of structure from motion photogrammetry. Earth Surf. Process. Landforms 42, 473–486. https://doi.org/10.1002/esp.4012

Collin, A., Archambault, P., Long, B., 2008. Mapping the shallow water seabed habitat with the SHOALS, in: IEEE Transactions on Geoscience and Remote Sensing. https://doi.org/10.1109/TGRS.2008.920020

Cramer, M., Stallmann, D., Haala, N., 2000. Direct georeferencing using gps/inertial exterior orientations for photogrammetric applications. Int. Arch. Photogramm. Remote Sens. https://doi.org/10.1017/CBO9780511777684

Dham, V.-T.I., 2017. Programming Chirp Parameters in TI Radar Devices Application, Report [WWW Document]. URL http://www.ti.com/lit/an/swra553/swra553.pdf (accessed 1.3.19).

Domeneghetti, A., 2016. On the use of SRTM and altimetry data for flood modeling in data-sparse regions. Water Resour. Res. https://doi.org/10.1002/2015WR017967

Durand, M., Fu, L.L., Lettenmaier, D.P., Alsdorf, D.E., Rodriguez, E., Esteban-Fernandez, D., 2010. The surface water and ocean topography mission: Observing terrestrial surface water and oceanic submesoscale eddies, in: Proceedings of the IEEE. pp. 766–779. https://doi.org/10.1109/JPROC.2010.2043031

Falco, G., Pini, M., Marucco, G., 2017. Loose and tight GNSS/INS integrations: Comparison of performance assessed in real Urban scenarios. Sensors (Switzerland). https://doi.org/10.3390/s17020255

Garambois, P.A., Calmant, S., Roux, H., Paris, A., Monnier, J., Finaud-Guyot, P., Samine Montazem, A., Santos da Silva, J., 2017. Hydraulic visibility: Using satellite altimetry to parameterize a hydraulic model of an ungauged reach of a braided river. Hydrol. Process. https://doi.org/10.1002/hyp.11033

Giustarini, L., Matgen, P., Hostache, R., Montanari, M., Plaza, D., Pauwels, V.R.N., De Lannoy, G.J.M., De Keyser, R., Pfister, L., Hoffmann, L., Savenije, H.H.G., 2011. Assimilating SAR-derived water level data into a hydraulic model: A case study. Hydrol. Earth Syst. Sci. https://doi.org/10.5194/hess-15-2349-2011

Guenther, G.., 1981. Accuracy and penetration measurements from hydrographic trials of the AOL system, in: Proc. 4th Laser Hydrography Symposium. Salisbury, pp. 108–150.

Guenther, G.C., Cunningham, a G., Larocque, P.E., Reid, D.J., Service, N.O., Highway, E., Spring, S., 2000. Meeting the Accuracy Challenge in Airborne Lidar Bathymetry. EARSeL eProceedings 1, 1–27.

Höfle, B., Vetter, M., Pfeifer, N., Mandlburger, G., Stötter, J., 2009. Water surface mapping from airborne laser scanning using signal intensity and elevation data. Earth Surf. Process. Landforms. https://doi.org/10.1002/esp.1853

Hopkinson, C., Crasto, N., Marsh, P., Forbes, D., Lesack, L., 2011. Investigating the spatial distribution of water levels in the Mackenzie Delta using airborne LiDAR. Hydrol. Process. 25, 2995–3011. https://doi.org/10.1002/hyp.8167

Huang, Z.-C., Yeh, C.-Y., Tseng, K.-H., Hsu, W.-Y., Huang, Z.-C., Yeh, C.-Y., Tseng, K.-H., Hsu, W.-Y., 2018. A UAV–RTK Lidar System for Wave and Tide Measurements in Coastal Zones. J. Atmos. Ocean. Technol. 35, 1557–1570. https://doi.org/10.1175/JTECH-D-17-0199.1

Javernick, L., Brasington, J., Caruso, B., 2014. Modeling the topography of shallow braided rivers using Structure-from-Motion photogrammetry. Geomorphology.

https://doi.org/10.1016/j.geomorph.2014.01.006

Langhammer, J., Bernsteinová, J., Miřijovský, J., 2017. Building a high-precision 2D hydrodynamic flood model using UAV photogrammetry and sensor network monitoring. Water (Switzerland). https://doi.org/10.3390/w9110861

Lawford, R., Strauch, A., Toll, D., Fekete, B., Cripe, D., 2013. Earth observations for global water security. Curr. Opin. Environ. Sustain. 5, 633–643. https://doi.org/10.1016/j.cosust.2013.11.009

Leduc, P., Ashmore, P., Sjogren, D., 2018. Technical note: Stage and water width measurement of a mountain stream using a simple time-lapse camera. Hydrol. Earth Syst. Sci. 22, 1–11. https://doi.org/10.5194/hess-22-1-2018

LeFavour, G., Alsdorf, D., 2005. Water slope and discharge in the Amazon River estimated using the shuttle radar topography mission digital elevation model. Geophys. Res. Lett. 32, L17404. https://doi.org/10.1029/2005GL023836

Legleiter, C.J., 2012. Remote measurement of river morphology via fusion of LiDAR topography and spectrally based bathymetry. Earth Surf. Process. Landforms 37, 499–518. https://doi.org/10.1002/esp.2262

Mandlburger, G., Pfeifer, N., Soergel, U., 2017. Water Surface Reconstruction In Airborne Laser Bathymetry From Redundant Bed Observations, in: ISPRS Annals of the Photogrammetry, Remote Sensing and Spatial Information Sciences. https://doi.org/10.5194/isprs-annals-IV-2-W4-123-2017

Mandlburger, G., Pfennigbauer, M., Wieser, M., Riegl, U., Pfeifer, N., 2016. Evaluation Of A Novel Uav-Borne Topo-Bathymetric Laser Profiler. ISPRS - Int. Arch. Photogramm. Remote Sens. Spat. Inf. Sci. XLI-B1, 933–939. https://doi.org/10.5194/isprs-archives-XLI-B1-933-2016

Manfreda, S., 2018. On the derivation of flow rating curves in data-scarce environments. J. Hydrol.

https://doi.org/10.1016/j.jhydrol.2018.04.058

Maps.stamen.com, 2019. maps.stamen.com [WWW Document]. URL http://maps.stamen.com/#watercolor/12/37.7706/-122.3782 (accessed 10.11.19).

Montesarchio, V., Napolitano, F., Rianna, M., Ridolfi, E., Russo, F., Sebastianelli, S., 2015. Comparison of methodologies for flood rainfall thresholds estimation. Nat. Hazards. https://doi.org/10.1007/s11069-014-1357-3

Neeck, S.P., Lindstrom, E.J., Vaze, P. V., Fu, L.-L., 2012. Surface Water and Ocean Topography (SWOT) mission, in: Conference on Sensors, Systems and Next-Generation Satellites XVI. p. 85330G. https://doi.org/10.1117/12.981151

Noureldin, A., Karamat, T.B., Georgy, J., 2013. Fundamentals of inertial navigation, satellite-based positioning and their integration, Fundamentals of Inertial Navigation, Satellite-Based Positioning and their Integration. Springer. https://doi.org/10.1007/978-3-642-30466-8

Orbicon, 2018. Hydrometri.dk [WWW Document]. URL http://www.hydrometri.dk/hyd/ (accessed 12.12.18).

Ouédraogo, M.M., Degré, A., Debouche, C., Lisein, J., 2014. The evaluation of unmanned aerial system-based photogrammetry and terrestrial laser scanning to generate DEMs of agricultural watersheds. Geomorphology. https://doi.org/10.1016/j.geomorph.2014.02.016

Pai, H., Malenda, H.F., Briggs, M.A., Singha, K., González-Pinzón, R., Gooseff, M.N., Tyler, S.W., 2017. Potential for Small Unmanned Aircraft Systems Applications for Identifying Groundwater-Surface Water Exchange in a Meandering River Reach. Geophys. Res. Lett. https://doi.org/10.1002/2017GL075836

Pavelsky, T.M., Durand, M.T., Andreadis, K.M., Beighley, R.E., Paiva, R.C.D., Allen, G.H., Miller, Z.F., 2014. Assessing the potential global extent of SWOT river discharge observations. J. Hydrol. https://doi.org/10.1016/j.jhydrol.2014.08.044

Rao, S.-T.I., 2017. Introduction to mmwave Sensing: FMCW Radars [WWW Document]. URL https://training.ti.com/sites/default/files/docs/mmwaveSensing-FMCW-offlineviewing_3.pdf (accessed 1.3.19).

Rehak, M., Mabillard, R., Skaloud, J., 2013. A micro-UAV with the capability of direct georeferencing. Int. Arch. Photogramm. Remote Sens. Spat. Inf. Sci. https://doi.org/10.5194/isprsarchives-XL-1-W2-317-2013

Ridolfi, E., Manciola, P., 2018. Water level measurements from drones: A Pilot case study at a dam site. Water (Switzerland) 10. https://doi.org/10.3390/w10030297

Rossi, P., Mancini, F., Dubbini, M., Mazzone, F., Capra, A., 2017. Combining nadir and oblique uav imagery to reconstruct quarry topography: Methodology and feasibility analysis. Eur. J. Remote Sens. https://doi.org/10.1080/22797254.2017.1313097

Santise, M., Fornari, M., Forlani, G., Roncella, R., 2014. Evaluation of dem generation accuracy from UAS imagery, in: International Archives of the Photogrammetry, Remote Sensing and Spatial Information Sciences - ISPRS Archives. https://doi.org/10.5194/isprsarchives-XL-5-529-2014

Schneider, R., Tarpanelli, A., Nielsen, K., Madsen, H., Bauer-Gottwein, P., 2018. Evaluation of multi-mode CryoSat-2 altimetry data over the Po River against in situ data and a hydrodynamic model. Adv. Water Resour. https://doi.org/10.1016/j.advwatres.2017.11.027

Schumann, G., Matgen, P., Cutler, M.E.J.E.J., Black, A., Hoffmann, L., Pfister, L., 2008. Comparison of remotely sensed water stages from LiDAR, topographic contours and SRTM. ISPRS J. Photogramm. Remote Sens. 63, 283–296. https://doi.org/10.1016/j.isprsjprs.2007.09.004

Sidle, R.C., 2006. Field observations and process understanding in hydrology: Essential components in scaling. Hydrol. Process. https://doi.org/10.1002/hyp.6191

Styrelsen for Dataforsyning og Effektivisering, 2018. Aerial orthophoto [WWW Document]. URL https://download.kortforsyningen.dk/ (accessed 2.17.19).

Tarpanelli, A., Barbetta, S., Brocca, L., Moramarco, T., 2013. River discharge estimation by using altimetry data and simplified flood routing modeling. Remote Sens. https://doi.org/10.3390/rs5094145

Tauro, F., Selker, J., Van De Giesen, N., Abrate, T., Uijlenhoet, R., Porfiri, M., Manfreda, S., Caylor, K., Moramarco, T., Benveniste, J., Ciraolo, G., Estes, L., Domeneghetti, A., Perks, M.T., Corbari, C., Rabiei, E., Ravazzani, G., Bogena, H., Harfouche, A., Broccai, L., Maltese, A., Wickert, A., Tarpanelli, A., Good, S., Lopez Alcala, J.M., Petroselli, A., Cudennec, C., Blume, T., Hut, R., Grimaldia, S., 2018. Measurements and observations in the XXI century (MOXXI): Innovation and multi-disciplinarity to sense the hydrological cycle. Hydrol. Sci. J. 63, 169–196. https://doi.org/10.1080/02626667.2017.1420191

Texas Instruments, 2017. IWR1443 Single-Chip 76-to 81-GHz mmWave Sensor 1 Device Overview [WWW Document]. URL http://www.ti.com/lit/ds/symlink/iwr1443.pdf (accessed 1.1.19).

Turner, D., Lucieer, A., Wallace, L., 2014. Direct georeferencing of ultrahigh-resolution UAV imagery. IEEE Trans. Geosci. Remote Sens. 52, 2738–2745. https://doi.org/10.1109/TGRS.2013.2265295

Wackrow, R., Chandler, J.H., 2011. Minimising systematic error surfaces in digital elevation models using oblique convergent imagery. Photogramm. Rec. 26, 16–31. https://doi.org/10.1111/j.1477-9730.2011.00623.x

Westaway, R.M., Lane, S.N., Hicks, D.M., 2001. Remote sensing of clear-water, shallow, gravel-bed rivers using digital photogrammetry. Photogramm. Eng. Remote Sensing 67, 1271–1281.

Westaway, R.M., Lane, S.N., Hicks, D.M., 2000. The development of an automated correction procedure for digital photogrammetry for the study of wide, shallow, gravel-bed rivers. Earth Surf. Process. Landforms 25, 209–226. https://doi.org/10.1002/(SICI)1096-9837(200002)25:2<209::AID-ESP84>3.0.CO;2-Z

Wohl, E., 2017. The significance of small streams. Front. Earth Sci. https://doi.org/10.1007/s11707-

017-0647-y

Woodget, A.S., Carbonneau, P.E., Visser, F., Maddock, I.P., 2015. Quantifying submerged fluvial topography using hyperspatial resolution UAS imagery and structure from motion photogrammetry. Earth Surf. Process. Landforms 40, 47–64. https://doi.org/10.1002/esp.3613

Young, D.S., Hart, J.K., Martinez, K., 2015. Image analysis techniques to estimate river discharge using time-lapse cameras in remote locations. Comput. Geosci. https://doi.org/10.1016/j.cageo.2014.11.008